Multi-scale variations of hydro-mechanical conditions at the base of the surge-type glacier Kongsvegen, Svalbard

Coline Bouchayer[1,2], Ugo Nanni[2], Pierre-Marie Lefeuvre[3], John Hulth[2], Louise Steffensen Schmidt[2], Jack Kohler[3], François Renard[1,4], and Thomas V. Schuler[2]

[1]The Njord Centre, Departments of Geosciences and Physics, University of Oslo, 0316 Oslo, Norway
[2]GeoHyd section, Department of Geosciences, University of Oslo, 0316 Oslo, Norway
[3]Norwegian Polar Institute, Tromsø, Norway
[4]ISTerre, Univ. Grenoble Alpes, Grenoble INP, Univ. Savoie Mont Blanc, CNRS, IRD, Univ. Gustave Eiffel, 38000 Grenoble, France

Correspondence: Coline Bouchayer (colili@uio.no)

Abstract. Fast glacier flow and dynamic instabilities, such as surges, are primarily caused by changes at the ice-bed interface, where basal slip and sediment deformation drive basal glacier motion. Determining subglacial conditions and their responses to hydraulic forcing (e.g. rainfall, surface melt) remains challenging due to the difficulty of accessing the glacier bed. In this study, we monitor the interplay between surface runoff and hydro-mechanical conditions at the base of the Arctic surge-type glacier

5   Kongsvegen, in Svalbard, over two contrasting melt seasons. Kongsvegen last surged in 1948, after which it entered a prolonged quiescent phase. Around 2014, flow speeds began to increase, sign of an imminent new fast-flow event. In 2021 we instrumented a borehole to assess subglacial conditions at the local scale and deployed seismometers to monitor the subglacial conditions at the kilometer scale. We measure both subglacial water pressure within the borehole with a water pressure sensor and till rheology with a ploughmeter inserted into the sediments at the bottom of the borehole. We use channel-flow-induced tremors

10 recorded by a seismometer to characterize hydraulic conditions over a kilometre scale at the base of the glacier. The records cover the period from spring 2021 until summer 2022. To characterize the variations in the subglacial conditions caused by changes in surface runoff, we investigate the phase relationship (i.e. how two variables evolve in time) of the following hydro-mechanical condition proxies: water pressure, hydraulic gradient, hydraulic radius, and sediment ploughing forces. We analyse these proxies versus modelled runoff analyzed over seasonal, multi-day and diurnal time-scales. We compare our results with

15 existing theories in terms of subglacial drainage system evolution and sediment shear strength to describe various aspects of subglacial conditions. We find apparent ambiguities in the interpretation of different variables recorded by individual sensors, thus demonstrating the importance of using multi-sensor records in a multi-scale analysis. This study highlights the different adaption of the subglacial drainage system during short, low melt intensity season in 2021, against long, high intensity melt season in 2022. In the short and low intensity melt season, we find that the subglacial drainage system evolves at equilibrium

20 with runoff, increasing its capacity as the melt season progresses. In contrast, during the long and high intensity melt season 2022, we find that the subglacial drainage system evolves transiently to respond to the abrupt and high intensity input of precipitation and melt water conveyed to the bed. In this configuration, the subglacial channels evolution is not rapid enough to adapt immediately to the forcing conditions. The drainage capacity of the main active channels is exceeded, promoting the

water to leak in poorly connected areas of the bed, increasing the water pressure, resulting in speed-up events. Another robust
outcome of our analysis is, that, on a seasonal scale, till shear strength variations are mainly anti-correlated with water pressure
variations (consistent with a Coulomb-plastic behavior), whereas on shorter time scales especially during speed-up events, the
two variables correlate, describing a viscous rheology. To our knowledge, such contrasted behaviors of the sediment rheology
and subglacial flow at the base of a glacier have not been reported before.

1 Introduction

Glacier ice loss represents one of the greatest global environmental risks in a warming climate due to its contribution to sea
level rise (Moon et al., 2018; Rounce et al., 2023), but currently, models are deficient in explaining dynamic responses and
instabilities such as surges (Lenton et al., 2008; Flowers, 2015; Benn et al., 2019; Thøgersen et al., 2019). Glacier flow is
controlled by (i) viscous deformation of the ice (e.g., Millstein et al., 2022), (ii) slip at the ice-bed interface (e.g., Zoet et al.,
2022), and (iii) subglacial sediment deformation (e.g., Minchew and Meyer, 2020). Basal processes (ii and iii) are responsible
for most of the short-term velocity variations and rapid ice flow (Thøgersen et al., 2019; Gilbert et al., 2022) but are still poorly
understood due to the difficulty in observing the subglacial environment. Unravelling the response of subglacial conditions to
surface water input and its consequences for glacier dynamics is key to reduce uncertainties in future projections of ice mass
loss to the oceans (Stocker, 2014; Pörtner et al., 2019; Maier et al., 2022).

A prominent example of coupled changes of subglacial conditions and glacier motion is that of glacier surges. Surge-type
glaciers exhibit quasi-cyclic phases of rapid flow, called the surge, after a long period of slow movement called the quiescent
phase (Meier and Post, 1969; Truffer et al., 2021). Due to the inability to efficiently transport accumulated mass to the ablation
area, the reservoir area of the glacier builds up mass during quiescence, resulting in steepening the glacier surface. As a
consequence, the gravitational driving stress increases, and at some point a threshold is reached, enabling fast flow. This
threshold has been proposed to depend on the degree of cavitation at the glacier base (Iken, 1981; Kamb, 1987; Thøgersen
et al., 2019) or till (i.e., subglacial sediments) shear strength (Iverson et al., 1995; Clarke, 2005; Minchew and Meyer, 2020;
Zoet and Iverson, 2020). It thus depends on basal water pressure (hereafter, referred to as water pressure) and on the evolution of
the subglacial drainage system (Schoof, 2010; Gilbert et al., 2022). Such instabilities often originate locally but can propagate
and affect large parts of, or even the entire, glacier (Thøgersen et al., 2019).

Rates of basal motion depend on the gravitational driving stress imposed by the glacier geometry and frictional properties
of the glacier base which, in turn, are governed by the thermal regime and hydro-mechanical conditions. The rate of water
supply from the glacier surface and the state of the subglacial drainage system control the basal water pressure, hence basal
conditions are expected to vary on several time scales, inherited from typical variations of runoff and subglacial drainage
system evolution (e.g., Davison et al., 2019). Following the variation of surface energy balance and rainfall, glacier meltwater
runoff (hereafter, referred to as runoff) typically displays characteristic diurnal variations, superimposed on multi-day weather
cycles and a pronounced seasonality (Rothlisberger, 1987; Nienow et al., 2017; Schmidt et al., 2023). Variations in water
pressure are caused both by variations in runoff as well as by the state and evolution of bulk transmissivity of the subglacial

drainage system. Previous works have identified different components of the subglacial drainage system that conveys and stores water along the glacier bed. These include water sheets (Weertman et al., 1962), cavities in the lee of bedrock obstacles (Kamb, 1987), and channels incised into the ice or subglacial substrate (Röthlisberger, 1972; Nye, 1976; Hooke et al., 1990;
60 Walder and Fowler, 1994). Water sheets and cavity systems are spatially distributed across the glacier base, flow pathways are typically tortuous and these systems are characterized as hydraulically inefficient and often operate at high water pressures. In contrast, channelized drainage is highly localized and often hydraulically efficient, which permits fast flow of water and operates typically at low water pressures.

   Water pressure at the glacier base directly influences ice-bed coupling, as well as it affects shear strength of the till (Lliboutry,
65 1968; Clarke, 2005; Damsgaard et al., 2020; Zoet and Iverson, 2020; Hansen and Zoet, 2022; Tsai et al., 2022). This double-tracked influence gives rise to complex behavior in the relationship between water pressure and basal motion, with an exact formulation still being debated (Benn et al., 2019; Thøgersen et al., 2019; Terleth et al., 2021; Gimbert et al., 2021a; Gilbert et al., 2022). Whereas high water pressure weakens the ice-bed coupling and therefore promote sliding, low water pressure has the opposite effect. In addition, pressure-gradient driven transport of water into or out of the till pore space affects rheological
70 properties of the till and thus influence rates of sediment deformation (Iverson et al., 1995; Hooke et al., 1997; Tulaczyk et al., 2000; Hansen and Zoet, 2022; Warburton et al., 2023). To date, the fundamental nature of till rheology is still debated and both Coulomb-plastic, linear-viscous and non-linear rheologies have been proposed (Alley et al., 1986; Boulton and Hindmarsh, 1987; Fischer et al., 1998, 2001; Kavanaugh and Clarke, 2006). Subglacial properties may exert a strong control on glacier stability so constraining till rheology is fundamental to understand the dynamic of e.g., glacier surges.

75   To investigate subglacial properties, boreholes measurements have provided direct access to the glacier bed and have often been instrumented to monitor water pressure (e.g. Hubbard et al., 1995; Sugiyama et al., 2011; Andrews et al., 2014; Doyle et al., 2018; Sugiyama et al., 2019; Rada and Schoof, 2018; Rada Giacaman and Schoof, 2023). Studies based on numerous boreholes highlighted the simultaneous and different behaviour experienced by different areas of the bed. Such processes are yet poorly described by current drainage models (Flowers, 2015). For example, some areas of the glacier bed can be connected
80 to the main subglacial drainage pathway, whereas other parts are not, and further areas even display alternating behavior (e.g., Gordon et al., 1998; Kavanaugh and Clarke, 2000). Further studies pointed-out that some areas of the bed show signs of hydraulic isolation (e.g., Murray and Clarke, 1995; Andrews et al., 2014; Hoffman et al., 2016; Rada and Schoof, 2018). Many long-term observations have a marked spatial heterogeneity of water pressure variations, even at small spatial scales (Murray and Clarke, 1995; Iken and Truffe, 1997; Fudge et al., 2008; Andrews et al., 2014; Rada and Schoof, 2018), as well as sudden
85 changes, indicative for reorganisation of drainage system (Gordon et al., 1998; Kavanaugh and Clarke, 2000). Further borehole instrumentation has been used to collect information on till shear strength using ploughmeters inserted into the till layer, on sliding rates using drag spools and on till deformation using inclinometers (e.g., Fischer and Clarke, 1994; Fischer et al., 1998, 1999, 2001; Porter et al., 1997; Kavanaugh and Clarke, 2000). Borehole studies have therefore provided crucial information on the local hydro-mechanical adaptation of the subglacial environment to changes in runoff and the following impact
90 on glacier dynamic. Due the co-existence of different subglacial drainage system components and their dynamic evolution over time, the interpretation of the hydro-mechanical conditions variations from borehole studies solely remain very local and

challenging to extrapolate at glacier-scale. Recent studies have shown the potential of using cryoseismology to bridge the gap between observations at different scales (Podolskiy and Walter, 2016), for instance by inferring hydraulic conditions across various temporal (sub-daily to multi-year) and spatial (decametric to kilometric) scales (Bartholomaus et al., 2015; Gimbert

95 et al., 2016; Nanni et al., 2020; Lindner et al., 2020; Labedz et al., 2022). This is based on the principle that turbulent water flow generates seismic tremor at high frequency (>1 Hz) can be used to quantify relative changes in the subglacial drainage system conditions (Gimbert et al., 2016). The recorded seismicity is mainly dominated by the strongest seismic sources and thus often represents the most active part of the drainage system (Nanni et al., 2021). The wide range of methods used to investigate subglacial condition highlights the need to collect various proxies of hydro-mechanical conditions to understand

100 the feedback between the development of the subglacial drainage system, rheological changes in the till and consequences for basal motion.

In this study, we present the results of a comprehensive, subglacial multi-sensor record, complemented by a cryoseismological dataset, all simultaneously acquired at Kongsvegen, a surge-type glacier in Svalbard. The field instrumentation has been designed to optimize interpretation by co-locating the instruments in a single borehole and accompanying measurements of

105 glacier surface velocity and energy-balance driven estimates of surface runoff. The records span the period from June 2021 to August 2022 and cover two contrasting melt seasons. Our results document runoff-induced variations in the subglacial hydro-mechanical conditions at different glaciologically significant time scales (diurnal, multi-day and seasonal). We discuss the implication of our findings in the context of glacier destabilization processes.

2 Field campaign and data collection

110 2.1 Study area

Kongsvegen glacier (hereafter, Kongsvegen, 78° 48'N, 12° 59' E) is located near Ny-Ålesund research station on the northwest coast of Svalbard (Fig. 1a). The glacier is $\sim$ 108km^2, $\sim$ 25.5 km long (in 2010, RGI, 2017) and ice thickness is $\sim$ 350 m at the drilling site (78° 18'N, 17° 13' E). The surface slope ranges from 0.5° to 2.5° with a north-western orientation (Hagen et al., 1993). The glacier drains into Kongsfjorden and its terminus is grounded below sea level. Typical for an Arctic glacier, its ice

115 is polythermal with a temperate base and an upper layer of 50-130 m thick cold ice. Ice in the accumulation zone is temperate while it is frozen to the lateral margins in the ablation zone (Björnsson et al., 1996). The glacier rests on fine-grained sandstone and sand/silt (Hjelle, 1993).

Kongsvegen is a surge-type glacier, with surges reported around 1800, 1869 and 1948 (Liestøl, 1988; Woodward et al., 2002). The glacier is in its quiescent phase since the last surge and exhibits low velocities of about 3 m a^{-1}. Melvold and Hagen

120 (1998) showed that the mass transported down glacier is only about 3-20% of the annual mass gained in the accumulation area, symptomatic for a surge-type glacier in its quiescent stage. Surface velocities recorded nearby the equilibrium line indicate that the glacier is accelerating since 2014, indicating the possibility for an imminent fast flow event (Fig. 1 b).

We conducted field campaigns to install and maintain a set of instruments at Kongsvegen starting in September 2020. Borehole and surface instrumentation was completed in April 2021 and the data collected cover the period from June 26, 2021

125 to August 8, 2022. The following section presents details about instrumentation and its usage.
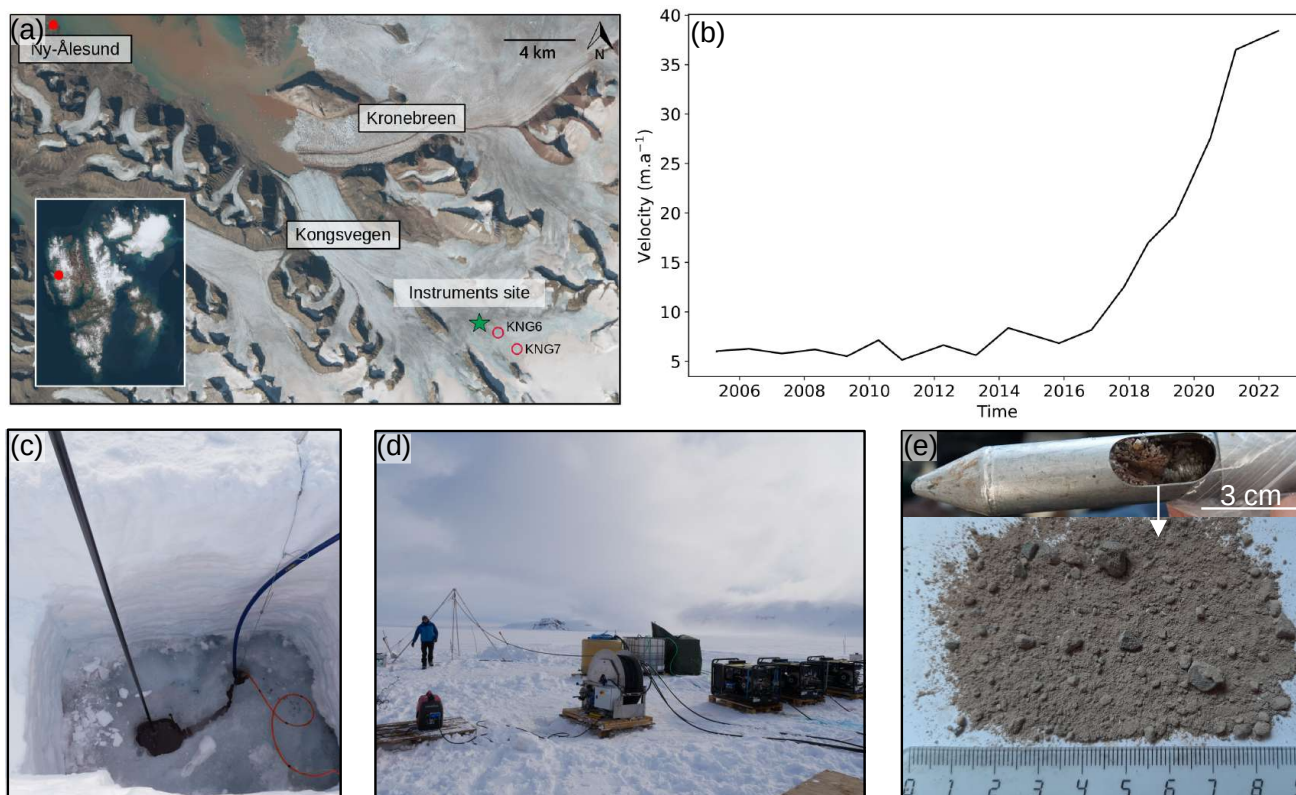
Figure 1. Study site and field methods. (a) Localisation of Kongsvegen in Svalbard. The green star indicates the instrument site where data were collected and the red circles indicate the position of the GNSS, KNG6, KNG7 (Credits: NPI/Copernicus Sentinel data). (b) Annual surface velocity near the equilibrium line of Kongsvegen glacier from 2005 to 2022, with an acceleration around 2014 witnessing that this glacier is close to a surge event. (c) Main borehole with the smaller secondary borehole where the return pump is installed. (d) Drilling installation. (e) Sediment sample recovered with a sediment sampling tool at the bottom of the borehole.

2.2   Borehole and surface instrumentation

On April 25, 2021, we drilled a borehole near the long term equilibrium line (78° 18'N, 17° 13' E, Fig. 1a) of Kongsvegen and placed instruments along the borehole and at its base. The borehole was drilled using a hot water drilling system, consisting of three high-pressure hot water machines (Kärcher HDS1000D), a 1/2 inch diameter high-pressure hose, a 2 m drill stem

130 with a 2.3 mm diameter nozzle, a pulley, a tripod, and water tanks (three 1000 liter IBC tanks, Fig. 1d). Since the glacier was

in winter conditions and liquid water was not available, water flowing out of the borehole was captured in an auxiliary hole for recycling (Fig. 1c). During drilling, the borehole water level started dropping when the drilling reached depth of 260 m, indicating a connection to an active drainage system. A sediment sample collected at the bottom of the $\sim$ 350 m borehole provides evidence for the existence of a sediment layer at the glacier bed (Fig. 1e).

135   At the bottom of the borehole, we installed a ploughmeter to monitor mechanical conditions of the subglacial till (e.g. Humphrey et al., 1993; Iverson et al., 1994; Fischer and Clarke, 1994; Porter et al., 1997; Fischer et al., 1998, 2001; Murray and Porter, 2001; Boulton et al., 2001). The ploughmeter is a 1.4 m long steel rod on which two strain gauges networks are mounted configured as two Wheatstone bridges, each composed of four strain gauges. The tip of the instrument penetrates into the till whereas its upper part remains in the borehole and is trapped in the ice. If the exact insertion depth of the device into the

140   till is unknown, from previous experiences with identical devices we estimate the penetration depth to be about 10 to 20 cm. As the glacier moves across its bed, the ploughmeter tip is dragged through the sediment, and the device bends which is sensed by the strain gauges. Just above the upper end of the ploughmeter, about 1 m above the glacier bed, we installed a vibrating wire pressure sensor (Geokon 4500SH, <2 kPa accuracy and 0.5 kPa resolution) to monitor water pressure, p. Sensor readings and data recording is performed using a Campbell Scientific CR1000X datalogger, recording data at one minute intervals.

145   One three-component geophone (DiGOS, 4.5 Hz) was installed into the ice at $\sim$1.5 m below the surface to ensure good coupling and to prevent melt-out during summer. DiGOS datacube, that comprises a digitizer and a datalogger, controlled the sampling rate (100 Hz) and recorded the signals. In this study, we analyse seismicity in the 3-10 Hz frequency band as a proxy for hydraulic conditions (Bartholomaus et al., 2015; Gimbert et al., 2016; Nanni et al., 2020; Lindner et al., 2020; Labedz et al., 2022). In addition, we used data of two surface stations (KNG6 and KNG7) that recorded positions using Global

150   Navigation Satellite System (GNSS), from which we derive daily surface velocities. The stations are located at distances of $\sim$ 700 m (KNG6 78.78067^{o}N, 13.15153^{o}E) and $\sim$ 3000 m (KNG7, 78.76770^{o}N, 13.23962^{o}E) upstream of the drill site. Data are recorded at five-seconds intervals continuously between April 1 and September 1 when there is enough sun for the solar panels, and to conserve battery power, only for one hour per day during the rest of the year. Static post-processing is applied to the GNSS data, assuming that the rover station is static for one hour due to the relatively low speed of the glacier. The Norwegian

155   Mapping Authority permanent network base station in Ny Ålesund is used as reference (baseline of $\sim$ 30 km). Gaps occurred in the data series when battery voltage was low, causing failure of the data logger. The two velocity records are merged, i.e. we consider the velocity derived from KNG6 when available and the one from KNG7 for the rest of the period (the original records for KNG6 and KNG7 can be seen in the Appendix A). We apply a one-week moving median for KNG7 velocity to smooth the record especially during the winter period when the velocities are low and thus the daily velocity derivation is less

160   accurate.

2.3 Surface runoff an meteorological conditions

The surface runoff is modelled using the CryoGrid community model (Westermann et al., 2022), coupling surface energy balance to a multi-layer snowpack model enabling simulation of glacier mass balance and freshwater runoff (Schmidt et al., 2023). The model is forced by 3-hourly fields of near surface conditions from the Copernicus Arctic Regional Reanalysis

165 (CARRA, Schyberg et al., 2020; Yang et al., 2021) for 2021 and forecasts by AROME-Arctic (Müller et al., 2017) for 2022. Meteorological forcings include 2 m air temperature and precipitation among other variables. CryoGrid community model then calculates the surface energy balance to simulate the mass balance components as well as the build-up and decay of seasonal snow. The available surface water from melt or rainfall percolates into snow and firn where it is retained, refreezes or runs off. The latter quantity corresponds to the runoff, Q, used in this study. Q is modelled on a 2.5 by 2.5 km grid and we assume that

170 all runoff produced upstream of our borehole is conveyed through the 6.25 km^2 surface area around our borehole without any delay. The temporal resolution of the runoff output is three hours. A complete description of the workflow is given by Schmidt et al. (2023).

3 Method

3.1 Derivation of subglacial variables

175 #### 3.1.1 Calculation of ploughmeter force

Based on the calibration performed in the laboratory prior to field deployment, we calculate the force experienced by the ploughmeter while being dragged through the sediment, referred to as force, F. To perform the calibration, loads were applied to the horizontally fixed ploughmeter by hanging a known mass on its free end. We repeated these measurements in eight orientations (0 to 315° every 45°) using masses of 10 kg and 50 kg corresponding to loads of ∼100 and ∼500 N, respectively.

180 The strain gauges on the ploughmeter are measured using a Wheatstone bridge for each pair in X and Y directions (Hoffmann, 1974). The datalogger records signal voltages Vx and Vy and the excitation voltage across at each bridge. After applying the calibration, we derive F from the X and Y components using Pythagoras' theorem.

3.1.2 Calculation of the channel-flow-induced seismic power, hydraulic radius and hydraulic gradient

From the recorded seismicity, we derive the seismic power, P, in a frequency band indicative of turbulent water flow, (3 to 10

185 Hz, Nanni et al., 2020). Variations in this frequency band are related to changes in hydraulic radius, R, i.e. the ratio of the cross-sectional area of the channel flow to its wetted perimeter, and in hydraulic gradient, S, i.e. the water pressure gradient in the along flow direction. For open channel flow, R scales with flow depth and S with channel slope. For glaciers, Gimbert et al. (2016) expressed P as a function of R and S. The total runoff, Q, depends on the fraction of runoff in individual channels and the number of channels, N. All channels are assumed to have identical R and S. The relative changes of these variables are

190 derived from relative changes in P and Q (Gimbert et al., 2016):

$$\frac{S}{S_{ref}} = \left(\frac{P}{P_{ref}}\right)^{24/41} \left(\frac{Q}{Q_{ref}}\right)^{-30/41} \left(\frac{N}{N_{ref}}\right)^{6/41} \tag{1}$$

$$\frac{R}{R_{ref}} = \left(\frac{P}{P_{ref}}\right)^{-9/82} \left(\frac{Q}{Q_{ref}}\right)^{-21/41} \left(\frac{N}{N_{ref}}\right)^{-33/82} \qquad (2)$$

where the subset ref represents a reference state that must be defined over the same period for Q and P, but not necessarily

195   for R and S. In our case, the reference state was taken on June 24, 2021 ($Q_{ref} = 0.08$ m^3 s^{-1} and $P_{ref} = 180.59$ dB) which

corresponds to the pre-melt season 2021 value against which we want to evaluate relative changes happening during the melt

season. The last term in both equations equals unity because we assume a constant N. For very small values of Q and P,

their negative exponents inhibit derivation of meaningful values for R/R_{ref} and S/S_{ref}. The method is described in detail by

Gimbert et al. (2016). To simplify notation, we hereafter refer to R/R_{ref} and S/S_{ref} as R and S respectively.

200   We evaluate our results against theoretical considerations relating P and Q (Gimbert et al., 2016), and hydraulic properties

and Q (Röthlisberger, 1972; Nanni et al., 2020) to discuss the state of the subglacial drainage system during the period of our

records. The scaling relationship proposed by Gimbert et al. (2016) defines cases where steady-state channels incised in the

ice adapt to changes in Q by only adjusting R (constant S) or the opposite case (constant R). Nanni et al. (2020) adapted

Röthlisberger's (1972) theory to derive scaling relationships between R and Q, and S and Q, both for a steady-state channel

205   evolution incised in the ice as well as for a channel of static cross-section evolving thus as a rigid pipe (Table 1).

Table 1. Scaling relationships between P and Q, S and Q, and R and Q for special cases, derived by Gimbert et al. (2016) and Nanni et al. (2020) from Röthlisberger (1972) theory to assess the state of channel variations.

Context	Relation	Reference
Change in runoff occurring at constant hydraulic radius	$P \propto Q^{14/3}$	Gimbert et al. (2016)
Change in runoff occurring at constant hydraulic gradient	$P \propto Q^{5/4}$	
Steady-state channel	$R \propto Q^{9/22}$	Röthlisberger (1972); Nanni et al. (2020)
	$S \propto Q^{-2/11}$	

3.2   Processing of time series, catalog of events and classification

Our analysis is based on the premise that changes in runoff induce changes in water pressure and till rheology. To characterize

the responses of the subglacial environment to runoff, Q, we analyse the responses of the subglacial variables recorded in

the present study, i.e. the force, F, the water pressure, p, the channel-flow-induced seismic power, P, the hydraulic radius,

210   R and the hydraulic gradient, S, in terms of phase relationship to Q. Here we use the term phase to characterize the time

relationships between one of the subglacial variables and events detected in the time series of Q. These phase relationships are

analysed at three different, glaciologically significant time scales: seasonal, multi-day, and diurnal. To extract the corresponding

components at these three time scales, the time series are filtered using a low-pass filter with cutoff at 20 days, a band-pass

filter between four and eight days, and a band-pass filter between six hours and 36 hours, respectively. We subdivide the multi-

215   day and diurnal time series into individual events based on Q variations. An event is defined by two subsequent minima of

Q. We normalize both Q and the subglacial variables by their respective maxima and subdivide the time into 50 equidistant
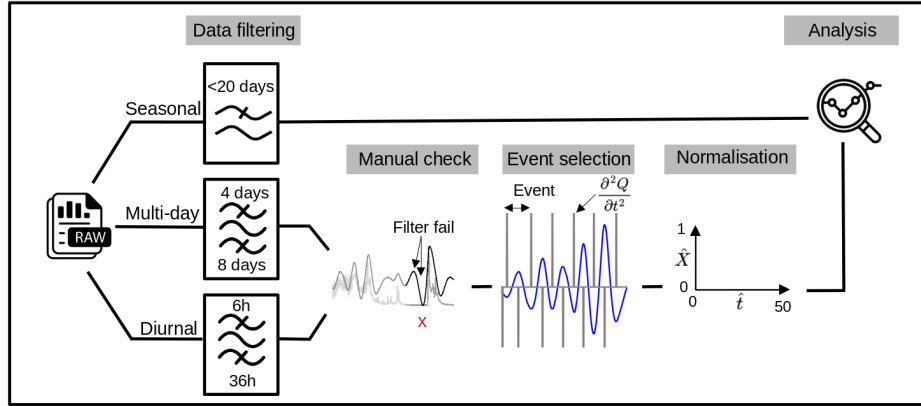
Figure 2. Preprocessing workflow applied to the time series. The original time-series (see Fig. 4 below) have been filtered at three time-scales. The multi-day and diurnal filtered data have been inspected against the unfiltered data to remove spurious artefacts that can be created by the filtering technique (see also Appendix E, E1). We then segmented the recorded data into multiple events and normalised the magnitude and duration of each.

steps. The number of time steps was chosen empirically as the minimum number of data points that preserves the shape and characteristics of the event time series (Fig. 2). We synthesize the different responses of each subglacial variables to changes in Q using a classification scheme (Fig. 3). Our workflow resembles that developed by Nanni et al. (2020) to understand sub-
220 glacial hydrology on hard-bed glaciers, and by Javed et al. (2021) to study storm-induced hydrological conditions variations. The period of records is subdivided; at a multi-day time scales into twelve events (melt season 2021, see Appendix B, Tab. B1) and eight events (melt season 2022, see Appendix B, Tab. B2); and at a diurnal time scale into 96 events (melt season 2021, see Appendix B, Tab. B3) and 85 events (melt season 2022, see Appendix B, Tab. B4).

Our classification scheme is based upon the following metrics: the slope m of the linear regression between the subglacial
225 variable X (with X being F, P, p, R or S) and Q (black line, Fig. 3); the squared residuals, RSS, between the linear regression and the $X_{norm} - Q_{norm}$ hysteresis loop; θ whose sign indicates the direction of the hysteresis loop. The spread of the data relative to the regression is quantified by (Appendix D, Fig. D1b):

$$RSS = \sum_{i=1}^{n} r_i^2 \tag{3}$$

where r_i are the residuals of the regression.

230 The parameter θ expresses the asymmetry of the response with respect to the forcing and its sign determines whether the hysteresis is clockwise or counterclockwise. We compute θ by comparing the mean of the subglacial variable considered during the rising limb of Q, $\overline{X}_{Q_{rising}}$, to its counterpart during decreasing Q, $\overline{X}_{Q_{falling}}$ (Appendix D, Fig. D1a):

$$\theta = \frac{\overline{X}_{Q_{rising}} - \overline{X}_{Q_{falling}}}{\overline{X}_{Q_{falling}}} \tag{4}$$
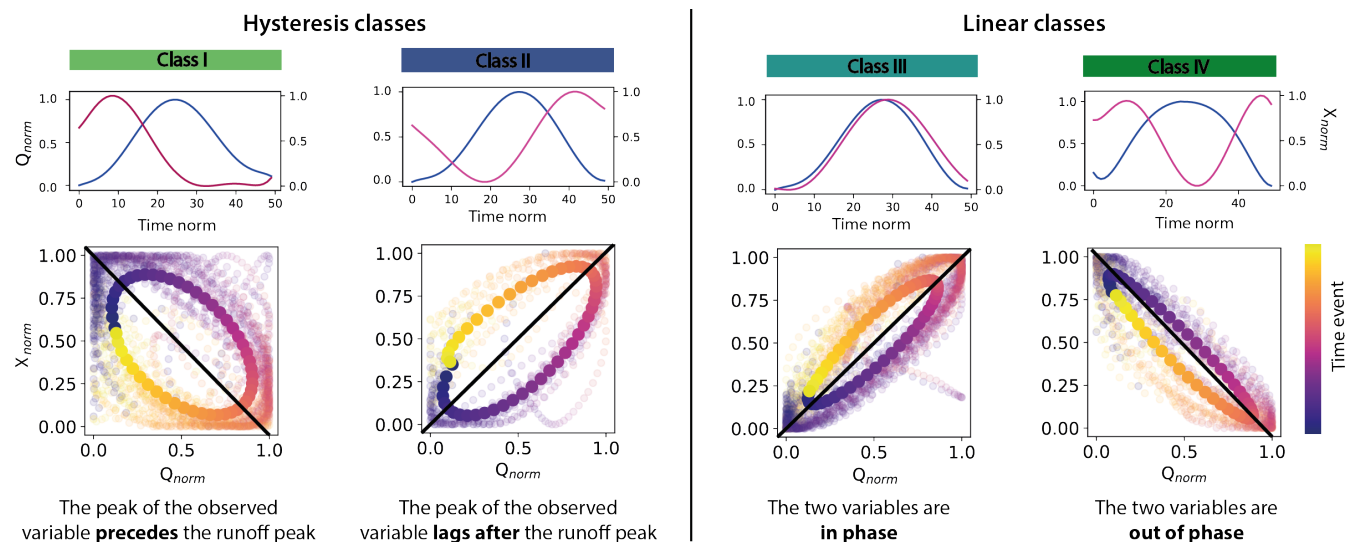
Figure 3. Phase relationship classification for events. Below each class, the plots in the first row correspond to a representative event for this class with runoff (Q_{norm}) plotted in blue and one subglacial variable (X_{norm}, with X being F, P, p, R or S) plotted in pink against time. The magnitude of the variables is normalised between 0 and 1 and the time is re-sampled into 50 time steps. The plots in the second row show the shape of the relationship between the two variables after classification. The solid color points refer to the mean behavior in this class, all individual events from the filtered time series are shown in shaded colors. The black line is the linear regression fitted to the scatter plot. Classes I and II correspond to clockwise or anti-clockwise hysteresis (or time-lag) between the runoff, Q, and the observed variable, while classes III and IV correspond to linear relationships. The color scale indicates chronology.

The sign of θ indicates whether the signal precedes ($\theta > 0$) or lags ($\theta < 0$) Q. Events are classified according to the phase
235   relationship between Q and the subglacial variable. We distinguish four classes, representing the following cases (Fig. 3):

- Class I: The subglacial variable considered precedes Q, $RSS > 2$ & $\theta > 0$,

- Class II: The subglacial variable considered lags behind Q, $RSS > 2$ & $\theta < 0$,

- Class III: The subglacial variable considered and Q vary in phase, $RSS \leq 2$ & $m > 0$,

- Class IV: The subglacial variable considered and Q vary in anti-phase, $RSS \leq 2$ & $m < 0$.

240   To discriminate between linear and hysteresis relations, we use a threshold of $RSS = 2$, corresponding to a phase difference of about $\pi/10$ for two sinusoidal variations.
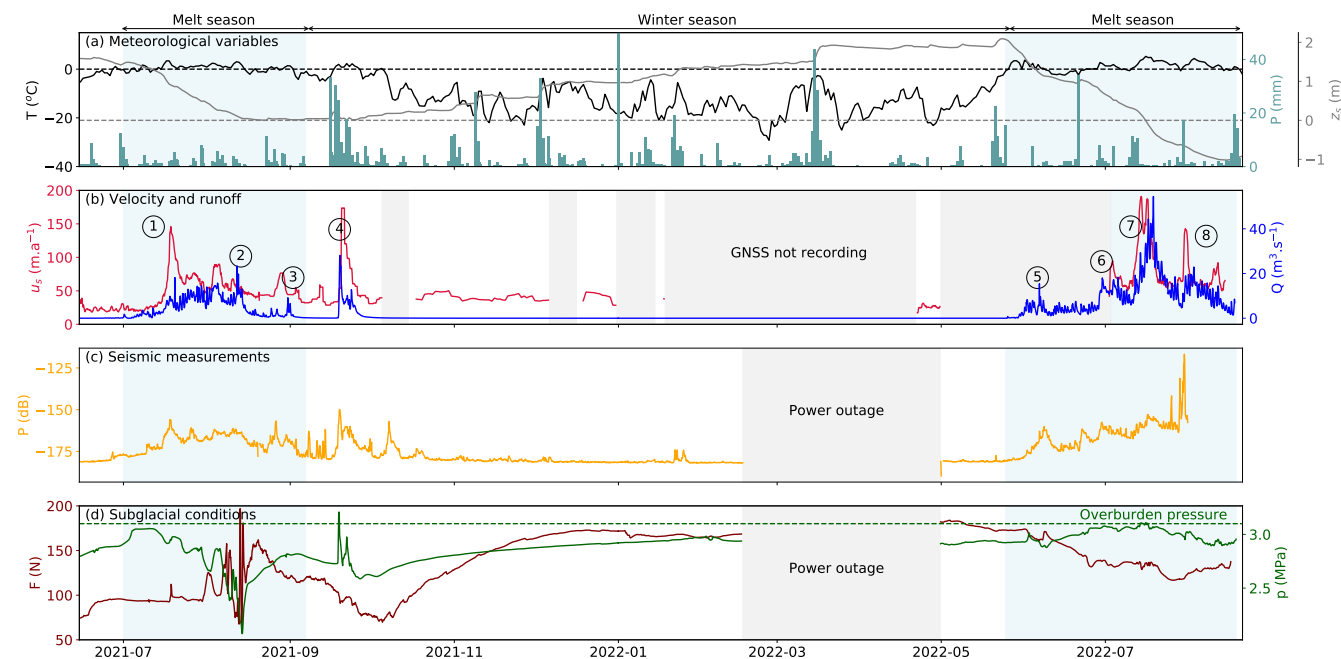
Figure 4. Time series of physical quantities measured from spring 2021 to summer 2022: (a) Temperature (black line), precipitation (light blue bars) from CARRA/AROME-Artic, and relative glacier surface height (grey line) from Cryogrid simulations (Schmidt et al., 2023). The three variables are extracted for the closest grid point of the borehole. In 2022, the surface height is negative which corresponds to ice melt. (b) Modelled runoff (blue line) and glacier surface velocity measured (red line). Circled numbers refer to different episodes described in the main text. (c) Channel-flow-induced seismic power recorded at the surface of the glacier in the 3-10 Hz frequency band (yellow line). (d) Borehole water pressure (green line) and force acting on the ploughmeter (dark red line). Blue shaded areas represent the melt seasons. Grey shaded areas represent periods of missing data.

4 Results

4.1 Overview over the dataset

The meteorological conditions extracted from CARRA/AROME-Arctic, the velocity, the runoff, Q, the channel-flow-induced
245 seismic power, P, the water pressure, p and the force acting on the ploughmeter, F, are displayed in Figure 4. We obtain time series covering two melt seasons (2021 and 2022) and one winter period. The meteorological conditions (Figure 4a) control timing and volume of Q resulting from meltwater production or rainfall (Figure 4b). We note that the dataset covers two very different melt seasons. While the 2021 melt season is short (67 days from July 1, 2021 to September 6, 2021), marked by low temperature oscillating around 0^oC and continuous low runoff (lower than 20 m^3 s^{-1}), the 2022 melt season is long (at
250 least 83 days because we do not capture the end of the melt season, from May 25, 2022 to August 16, 2022) marked by high temperatures (up to 7^oC) and frequent and large excursions of runoff above 20 m^3 s^{-1}. October 2021 marks the beginning

of the winter season highlighted by the drop in the temperature (Fig. 4a, black curve) and the increase in the relative surface height due to snowfall (Fig. 4a, grey curve).

In response to temperature and rainfall variations, Q displays variations on several glaciologically relevant time scales
255   (Fig. 4b, blue line): (i) the seasonal time scale (>20 days) is marked by Q generally being limited to the melt season; (ii) superimposed to this are variations on a multi-day time scale (four to eight days), typically reflecting weather variability (warm-spells, e.g., Fig. 4b②, or rainfall, e.g, Fig. 4b④); (iii) and being melt-dominated, Q reflects the pronounced diurnal variability of surface energy balance.

The channel-flow-induced seismic power P (Fig. 4c, yellow line) follows the variations in Q throughout the recorded period,
260   increasing at the beginning of the two melt seasons and decreasing towards their end. Such behaviour has been previously observed in other settings and confirms the sensitivity of the selected frequency band to Q (Bartholomaus et al., 2015; Gimbert et al., 2016; Nanni et al., 2020, 2021; Lindner et al., 2020; Labedz et al., 2022). In contrast, variations in water pressure in the borehole p do not follow Q variations in a simple way (Fig. 4d, green curve). At the beginning of the 2021 melt season, p is high, close to the overburden pressure. As Q continues to increase, p decreases until it reaches its minimum values ($\sim$2
265   MPa) after peak Q marked by ②. p increases again during the winter to reach a value (2.9 MPa) close to overburden pressure (3.2 MPa). In the second year of the record, p remains high and increases to the overburden pressure in mid-July 2022 before decreasing again to levels close to its winter value (2.9 MPa) at the end of August.

Similar to p, the force acting on the ploughmeter, F, shows different behaviors between the two melt seasons (Fig. 4d, dark red curve). During the melt season 2021, it remains fairly stable until August 2021, when it suddenly undergoes large amplitude
270   ($\sim$150 N maximum amplitude), high-frequency variations. As the instrument site become snow-free around the 15th of August 2021 (Fig. 4a), F gradually decreases towards the end of the melt season until it reaches its minimum value in early October 2021 ($\sim$ 70 N). At the end of September occurs a major precipitation episode (Fig. 4b④), with heavy rainfall going over to snowfall as the temperature dropped. F does not react to this event. After this precipitation event, F gradually increases until it stabilizes at $\sim$ 170 N in January 2022. Note that this value is almost twice the value observed before the melt season 2021
275   ($\sim$ 90 N).

The surface velocity of the glacier is related to Q-induced changes and several glacier speed-up episodes are identified early in the melt season 2021, when Q increased (Fig. 4b①), during large rainfall episode (Fig. 4b④), and during sudden influx of meltwater during the 2022 melt season (Fig. 4b, ⑥, ⑦, ⑧).

To interpret the responses of the subglacial drainage system and glacier dynamics to variations in runoff, Q, we analyze the
280   data using a phase relationship analysis on seasonal (above 20 days, Sec. 4.2), multi-day (four to eight days, Sec. 4.3), and diurnal (six hours to 36 hours, Sec. 4.4) time scales.

4.2   Analysis of seasonal variations

To examine the phase relationship between the subglacial variables and Q at the seasonal scale, all time series are low-pass filtered with a cut-off frequency of 20 days. We first describe the results obtained for the melt season 2021 and then for the
285   melt season 2022.
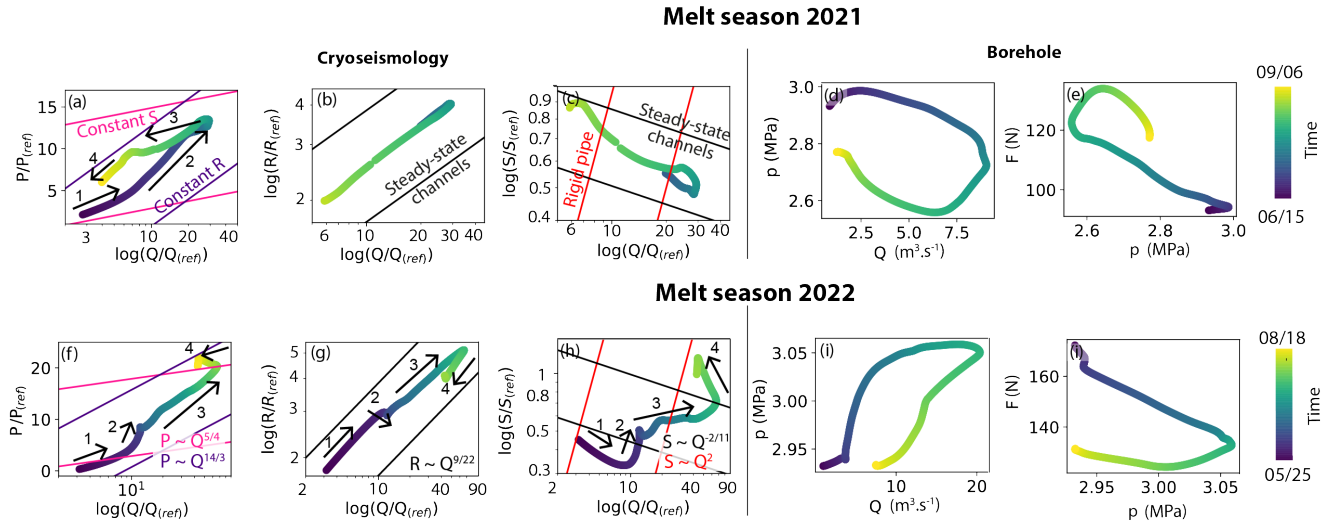
Figure 5. Relationships between two variables at the seasonal scale for the melt seasons 2021 and 2022. Color scales indicate the timing during both melt seasons. Note that the variables R and S have been derived only from July 19 to August 31, 2021 and from May 25 to August 1, 2022 explaining that the color scale is not entirely represented (outside of these periods, runoff is too low to derive R and S, see Section 3). P, R and S are expressed in terms of relative changes to a reference stage, in our case on June 14, 2021, when $Q_{ref} = 0.2\,\mathrm{m^3\,s^{-1}}$. (a) and (f) Relationships between scaled runoff (Q/Q_{ref}) and scaled channel-flow-induced seismic power (P/P_{ref}). The x-axis is in logarithmic scale. The superimposed lines show the relations derived by Gimbert et al. (2016) for a constant hydraulic gradient (pink lines, $P \propto Q^{5/4}$) and for a constant hydraulic radius (purple curve, $P \propto Q^{14/3}$). (b) and (g) Relationship between scaled runoff (Q/Q_{ref}) and scaled hydraulic radius (R/R_{ref}). x and y-axes are in logarithmic scale. Superimposed lines show the relations of steady-state channels evolution (Nanni et al. (2020), $R \propto Q^{9/22}$). (c) and (h) Relationship between scaled runoff (Q/Q_{ref}) and scaled hydraulic gradient (S/S_{ref}). x and y-axes are in logarithmic scale. Superimposed lines show the relations of Nanni et al. (2020) for a channel at steady-state (black lines; $S \propto Q^{-2/11}$) and for a channel evolving as a rigid pipe of static cross-section (red line; $S \propto Q^2$). (d) and (i) Relationship between water pressure and runoff. (c) and (j) Relation between force and water pressure. Arrows indicates the direction of time and numbers refer to different periods described in the main text.

We segmented the melt season 2021 into four regimes. At the beginning of the melt season, the channels evolve predominantly by adjusting R (constant S, Fig. 5a, 1). Shortly after, as Q increases, the channels predominantly evolve by adjusting S (constant R, Fig. 5a, 2). When Q decreases in August 2021, channels evolve at a constant S (Fig. 5a, 3). At the end of the melt season 2021, the channels switch regime again and evolve by adjusting S (Fig. 5a, 4). $R - Q$ trajectory is parallel

290   to the scaling relationships for channels evolving at steady-state (Fig. 5b) and we observe that S describe channels evolving at steady-state although $S - Q$ trajectory is not always strictly parallel to the scaling relationships (Fig. 5c). We observe that $p - Q$ relationship is characterised by a clockwise hysteresis loop (Fig. 5d) indicating that the peak in p precedes the peak in Q. The linear relationship between F and p indicates that the two subglacial variables are anti-correlated from June to August

2021 (Fig. 5e) and, at the end of the melt season, $F - p$ trajectory is a counter-clockwise hysteresis indicating the the peak in
F lags after the peak in p (Fig. 5e).

The melt season 2022 can be segmented into four regimes as for the melt season 2021 but these phases describe a different behaviour. At the beginning of the melt season, the channels evolve predominantly by adjusting R (Fig. 5f, 1), as observed in 2021. Then, the channels briefly leave this regime to follow an evolution that is not described by the theoretical predictions and that are not governed by a constant R or S (Fig. 5f, 2). They return to a regime predominantly governed by a constant R for the remaining increase in runoff phase (Fig. 5f, 3). The runoff decrease phase is not completely captured in the record because data do not contain the end of the melt season 2022. However, we observe that the channels evolution is not governed by a constant R or S (Fig. 5f, 4). We retrieve the four phases in the observation of R and S relationship with Q. During the phases 1 and 3, the channels evolve at equilibrium with Q (Fig. 5g and h, 1 and 3) and during the phases 2 and 4, the channels evolve closer to a rigid-pipe (Fig. 5g and h, 2 and 4). As opposed to the melt season 2021, the relationship between p and Q is linearly related (Fig. 5i). As for the melt season 2021, F and p are anti-correlated (Fig. 5j).

4.3 Analysis at multi-day scale
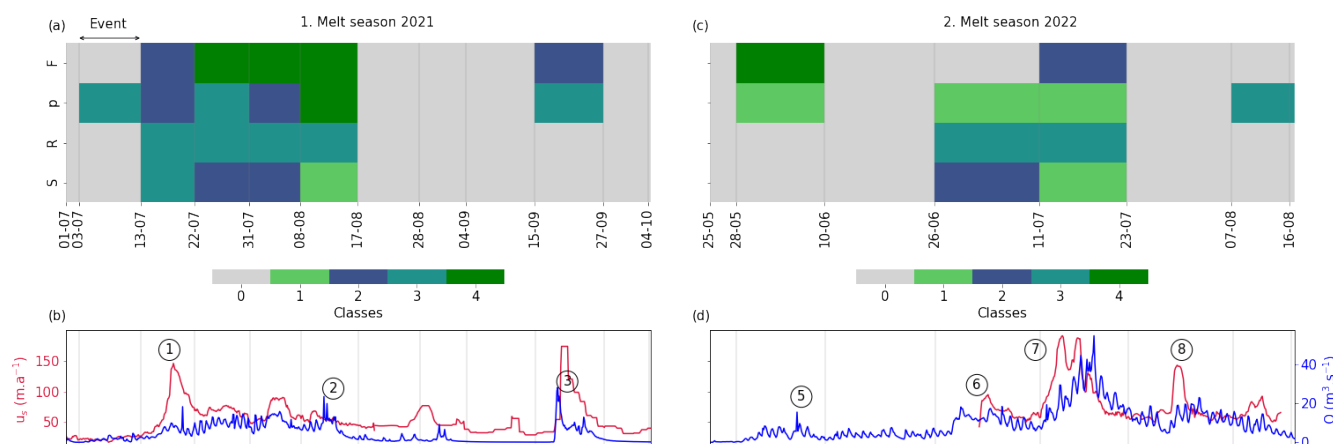
Figure 6. Phase relationships between the subglacial variables (S, R, p and F) and runoff (Q) at a multi-day time scale. (a) Classes from the phase relationship classification per event for the melt season 2021 and (c) for the melt season 2022. Grey fields refer to periods when data is missing and the vertical grey lines delineate the events. Classes I and II correspond to clockwise or anti-clockwise hysteresis between the runoff and the observed variable while classes III and IV correspond to linear relationships. (b) and (d) Variations in velocity (red line) and runoff (blue line) during the melt season 2021 and 2022 respectively. Circled numbers refers to episodes described in the main text.

To understand the relationships on time-scales of weather variations, we filtered the time series with a band-pass filter, removing the variations with periods below four days and above eight days. Then, we applied our phase relationship classification scheme to each events (Fig. 6). We investigate the phase relationships between the subglacial variables (the force, F, the water pressure, p, the hydraulic radius, R, the hydraulic gradient, S) and the runoff, Q, for each event during the 2021

(eleven events) and 2022 melt seasons (eight events, see Section 3). Similar phase relationships are observed during both melt seasons between (i) R and Q and (ii) S and Q. During both melt seasons, R evolves in phase with Q (class III, Fig. 6 a and c) as S at the beginning of the melt season 2021 (class III, Fig. 6a). We cannot compare the relationship between S and Q at the beginning of the melt season 2022 as we have removed the events due to the inconsistency between the filtered data and the raw data during this period (Appendix E, Fig. E1). For the remaining part of the season, the behaviour of S in response to Q is very similar in 2021 and 2022. During the first half of both melt seasons, S is first lagging after Q (class II, Fig. 6a and c). During Q important excursions occurring in August 2021 (Fig. 6b②) and July 2022 (Fig. 6d, ⑦), S precedes Q changes (class I, Fig. 6a and b). In contrast to R and S phase relationship to Q, F do not show the same time-evolution across both melt seasons but $F - Q$ phase relationship is sensitive to glacier acceleration. During high velocity episodes (Fig. 6b and d, ①, ③, ⑦), F systematically lags behind Q (class II, Fig. 6a and c). Conversely, when velocity is low and stable during the melt season 2021 (Fig. 6b and d, from ① to ③), F is anti-correlated with Q (Fig. 6a and c). We do not have GNSS data in 2022 at this period to compare with the observations in 2021. $p - Q$ phase relationship is contrasted between the melt season 2021 and 2022. On one hand, $p - Q$ phase relationship cannot be easily linked to specific Q regimes or speed-up episodes and shows various responses across the melt season 2021 (class II, III and IV, Fig. 6a and c). During the melt season 2022, p always precedes Q (class I, Fig. 6c).

Figure 7 shows the comparison between the multi-day scale observations of P, R and S and the scaling relationships by Gimbert et al. (2016); Nanni et al. (2020). At the beginning of the melt season 2021 (July 2021), the channels evolve at a constant R before switching to channels evolving at a constant S at the middle of the melt season (August 2021, Fig. 7a). At the end of the melt season, P switches back to an evolution governed by a constant R, similar to the beginning of the melt season 2021 (Fig. 7a). In general, R evolves with Q similar to what is expected for a steady-state channel (Fig. 7b) whereas S shows a more complex behaviour that is difficult to disentangle (Fig. 7c).

During the melt season 2022, the evolution of P is neither clearly dominated by a constant R or S (Fig. 7d). In general, R increases with Q but at a slope that differs from the one expected for steady-state channels (Fig. 7e). As in 2021, the evolution of S exhibits complex behaviour at this scale during the melt season 2022 (Fig. 7f).

4.4 Analysis of diurnal variations

Symptomatic for meltwater, the runoff, Q, exhibits strong diurnal variations. To examine the glacier response to changes in Q at a diurnal scale, we filtered the time series using a band pass filter, cutting off variations beyond the lower and upper limits of six hours and 36 hours, respectively (Fig. 8). The filtered time series are then subdivided into 95 events in 2021 and 84 events in 2022 (see Section 3) and we applied our phase relationship classification scheme.

We investigate the phase relationship between the subglacial variables (the force, F, the water pressure, p, the hydraulic radius, R, the hydraulic gradient, S) and Q on a diurnal time scale (Figs. 8a and b). We observe that R and S show consistent phase relationships with Q during both melt seasons, alternating between classes II and III, and classes I and IV, respectively (Fig. 3). However, $p - Q$ and $F - Q$ phase relationships vary across all classes without any easily identifiable pattern (Fig.
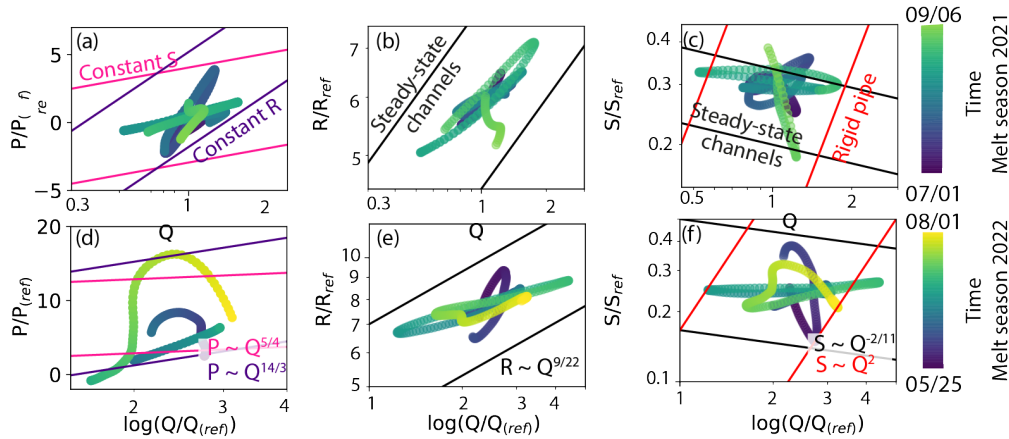
Figure 7. Relationship between the subglacial variables (P/P_{ref}, R/R_{ref}, S/S_{ref}) and runoff (Q/Q_{ref}) during the two melt seasons at a multi-day time scale. Color scale indicate the timing during both melt seasons and is scaled according to the length of each season. (a) and (d) Relationship between scaled runoff (Q/Q_{ref}) and scaled channel-flow-induced seismic power (P/P_{ref}). The x-axis is in logarithmic scale. The superimposed lines show the relations derived by Gimbert et al. (2016) for a constant hydraulic gradient (pink lines, $P \propto Q^{5/4}$) and for a constant hydraulic radius (purple curve, $P \propto Q^{14/3}$). (b) and (e) Relationship between scaled runoff (Q/Q_{ref}) and scaled hydraulic radius (R/R_{ref}). x and y-axis are in logarithmic scale. Superimposed lines show the relations of steady-state channels evolution (Nanni et al. (2020) $R \propto Q^{9/22}$). (c) and (f) Relationship between scaled runoff (Q/Q_{ref}) and scaled hydraulic gradient (S/S_{ref}). x and y-axis are in logarithmic scale. Superimposed lines show the relations of Nanni et al. (2020) for a steady-state channel evolution (black lines; $S \propto Q^{-2/11}$) and for a channel evolving as a rigid-pipe of static cross-section (red line; $S \propto Q^2$).

8a-c). The absence of clear diurnal variations in p and F is observed for much of the observation period (Appendix F, Fig. F1).

345   Therefore, we focus the analysis of diurnal variations on the responses of P, R and S.

During the 2021 melt season, we observe that R mostly varies in phase with Q (class III, Fig. 8a). S is mostly anti-correlated with or precedes Q (class I or IV, Fig. 8a).

During the melt season 2022, we observe a shift from linear responses of R and S (class III and IV, Fig. 8c) towards more hysteresis responses (classes I and II, Fig. 8c) when Q shows the first significant increase in June (Fig. 8c and d, ⑥). R varies

350   with changes in Q before this event (class III, Fig. 8c) but after, R lags behind Q (class II, Fig. 8c). Similarly, S shifts regimes from being anti-correlated with Q before the episode ⑥ (class IV, Fig. 8c) to a regime where S precedes Q after this period (class I, Fig. 8c).
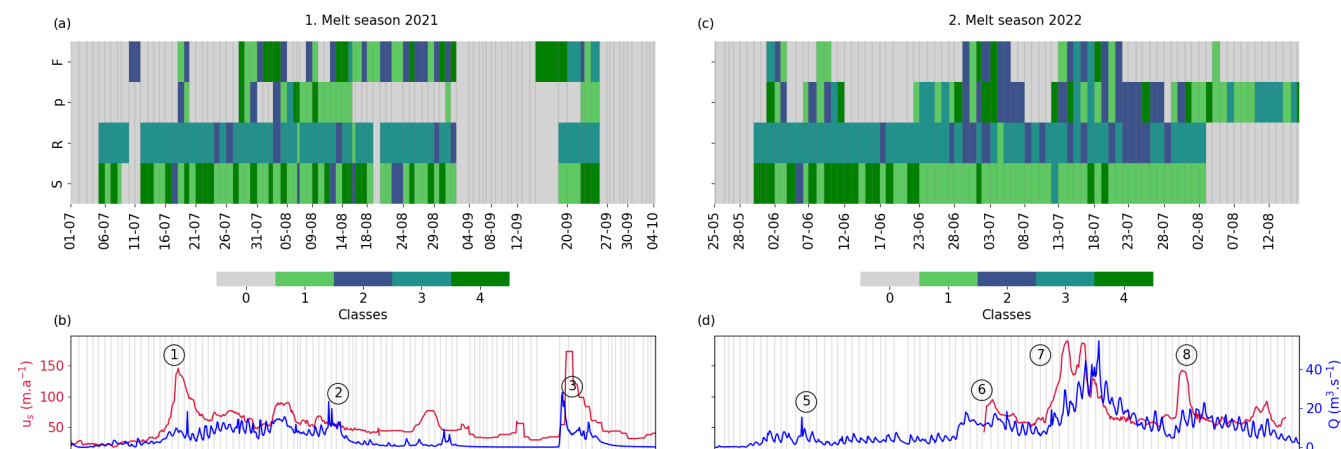
Figure 8. Phase relationship between the subglacial variables (S, R, p and F) and runoff (Q) at a diurnal time scale. (a) Classes from the phase relationship classification per event for the melt season 2021 and (c) for the melt season 2022. Grey fields refer to periods when data is missing and the vertical grey line delineate the events. Classes I and II correspond to clockwise or anti-clockwise hysteresis between the runoff and the observed variable, respectively, while classes III and IV correspond to linear relationships. (b) and (d) Variations in velocity (red line) and runoff (blue line) during the melt season 2021 and 2022, respectively. Circled numbers refer to episodes described in the main text.

5 Discussion

5.1 Interpreting the evolution of subglacial conditions

355 In this study, we have analyzed variations in subglacial hydro-mechanical conditions, i.e., the response of subglacial variables to changes in runoff and interpret now the observed behavior in terms of subglacial drainage system evolution (Sect. 5.2) and till rheology (Sect. 5.3). We classified the phase (i.e. time) relationships observed between different subglacial variables (the force, F, the water pressure, p, the hydraulic gradient, S, and the hydraulic radius, R) and runoff, Q, into four classes (Fig. 3). Here, we first consider the expected responses of R, S and p to changes in Q for different typical stages of subglacial channel

360 evolution. In addition, we discuss expected responses of F for different till rheologies. Second, we apply this interpretation scheme to the observed behavior separately for each of the considered time scales, before we consolidate these interpretations into a coherent picture of subglacial conditions.

Water flow is driven by the hydraulic gradient, and for a rigid pipe with constant cross-section, this results in a positive, linear $p - Q$ relationship (class III, Fig. 3). In this situation, we expect constant R, unaffected by variations in Q (not classified). Since

365 we always measure p at the same location and the glacier terminus is fixed at sea-level, we expect that variations in S are closely correlated to those of p. According to Röthlisberger's theory for ice-walled channels, the channel cross-section is determined by the counter-acting processes of melt opening due to dissipation of potential energy and creep-closure of the surrounding ice. In steady-state, these two processes balance each other, and, a larger runoff would be associated with a larger channel,

thus requiring lower S and p. This inverse $p - Q$ relationship is one of the best-known characteristics of ice-walled drainage.

370 Hence, we interpret a negative, linear relationship (class IV, Fig. 3) between Q and p (and similar for S and Q), as indicative for steady-state channel drainage. This situation also entails that R increases with Q (class III, Fig. 3). The evolution of the drainage system in response to Q typically is transient between the two end-members described above, with a static cross-section on one side and a fully-achieved steady-state on the other one. For transient evolution between these two end-members, a hysteresis behavior in the phase relationships between subglacial variables and Q is expected. Evolution towards steady-state

375 occurs after some time delay; if variations of the forcing term Q occur faster than this delay, the variations of R lag the variation of Q, resulting in a counter-clockwise hysteresis (class II, Fig. 3). For such a transient evolution, R is smaller during the rising limb of Q than during the decline, emanating as a counter-clockwise $R - Q$ hysteresis (class II, Fig. 3). At the same time, the larger R during the decline of Q requires a lower p to drive the flow, resulting in a clockwise hysteresis in the $p - Q$ relation (class I, Fig. 3). As stated above, we expect S to vary in a similar fashion as p. The response of channel-flow-induced seismic

380 power P to changes in Q is complex because it integrates the responses of both R and S, hence direct interpretation of the $P - Q$ relations is difficult.

Following Fischer and Clarke (1994) and Kavanaugh and Clarke (2006), for the interpretation of F variations experienced by the ploughmeter, we explore two different assumptions, each assuming a different till rheology. For a Coulomb-plastic till (Iverson et al., 1998), the shear strength depends directly on the pore-water pressure, which we assume to co-vary with p at

385 the bottom of the borehole. This behavior results in a negative, linear response of F to variations in p (class IV, Fig. 3). On the other hand, subglacial till may be considered as a linear-viscous material (Alley, 1990; Kamb and Engelhardt, 1991), requiring that F increases linearly with sliding velocity. Usually, glacier sliding laws acknowledge a water pressure control on sliding speed (Iken and Bindschadler, 1986; Hooke et al., 1997; Zoet and Iverson, 2020; Gilbert et al., 2022). In combination, this would result in a positive, linear relationship between F and p (class III, Fig. 3). However, more complex $F - p$ relationships

390 can emanate as well, accounting for that the relationship between p and sliding speed may be non-linear (Alley, 1989; Boulton and Hindmarsh, 1987). In general, interpreting a direct relation between F and Q is complicated by the circumstance that variations in p (and S) also depend on the efficiency of the drainage system to evolve to cope with runoff input, hence depend both on Q and R.

Our interpretation scheme described here lets us expect two to three options for the classification of phase relations between

395 each subglacial variable and Q. For $p - Q$ and $S - Q$, we expect behaviors according to classes I, III or IV; we expect $R - Q$ to display either class II or class III behavior; $F - p$ is expected to fall either in class III or class IV, direct $F - Q$ relations are not easily comprehended. In practice, we observe that some events are classified outside the expected range (Figs. 6 and 8). The occurrence of such behavior may be attributed partly to artifacts introduced by the spectral filtering applied to the time series for the analysis. Although we manually checked the consistency between the unfiltered and filtered signals to remove

400 the most apparent differences (see Section 3), some inconsistencies may still remain. Small shifts in timing of peaks may be amplified by normalizing the event time axis and hence lead to misclassification of some events. In addition, the definition of classes is based on somewhat arbitrarily selected thresholds (see Section 3), whereas the separation in reality may be distinct.

For instance, the linear classes III and IV still account for some degree of hysteresis (up to 20° of phase difference) and close to the thresholds, small differences may result in different classification.

5.2 Subglacial drainage system evolution

The two observed melt seasons considerably differ in terms of duration and intensity (Fig. 4). Whereas in 2021, melting occurs over a relatively short period and yields low levels of water supply, in 2022, the melt season lasts longer and is characterized by higher temperatures and thus yields higher water supply rates. This provides the opportunity to study the evolution of the subglacial drainage system in response to very different forcing.

5.2.1 The melt season 2021: short duration and low intensity

The melt season 2021 is short (67 days) and marked by runoff usually lower than 20 m^3 s^{-1} (Fig. 4a). Applying our interpretation scheme to the observed responses of the water pressure p, the channel-flow-induced seismic power P, the hydraulic radius R, and the hydraulic gradient,S, yields a largely consistent picture of a subglacial drainage system that fully adapts to seasonal runoff variations: $p-Q$ exhibits clockwise hysteresis, indicative of system capacity growing with runoff (Fig. 5d); $R-Q$ variations are positively-linearly related (Fig. 5b); the $S-Q$ relationship covers only the declining phase of Q and shows an increase of S during this decline, consistent with the above interpretation (Fig. 5c). As mentioned above, due to the composite nature of channel-flow-induced seismic power, $P-Q$ relationship is more difficult to interpret, but comparison to idealised behavior suggests that system adjustment is dominated by different mechanisms during different stages (Fig. 5a). Although all records draw the picture of a system adjusting to Q variations, there is a noteworthy difference in the interpretations of borehole measurements and those of cryoseismology records. While variations of R and S suggest that the system capacity obtains an equilibrium with Q for the long-term variations, the variations of p, measured in the borehole, indicate a transient evolution in response to changes in Q. $p-Q$ exhibits clockwise hysteresis, indicative of system capacity growing with runoff also this in agreement with expected behavior (Fig. 5d).

   Theoretical timescale of channel adjustment is typically longer (several days to weeks) than variations in Q (hours) (Röthlisberger, 1972). Channels at short time scale are then either overwhelmed when Q increases or partially filled when Q decreases which results into a channel evolution closer to a rigid pipe (constant channel cross-section) than steady-state channel (variable channel cross-section determined by the balance between melt opening and creep-closure to cope with runoff variations). We therefore expect a predominance of class III for the $p-Q$ and $S-Q$ relations on multi-day and diurnal time scales (Fig. 6a and 8a). The multi-day classifications of $p-Q$ and $S-Q$ relationship mainly support this view by displaying class II and III behavior (Fig.6a), however on diurnal time scales (Fig. 8a), the picture is less clear. On these shorter time scales, we expect only minor variations of R, lagging those of Q (class II). However, we observe mainly class III behavior at both multi-day and diurnal time scales (Fig. 6a and 8a), suggesting that geometrical adjustment of the drainage system takes place already over short time scales; however this implies that the observed behaviors of p and S are caused by changes in hydraulic roughness since R already has adjusted.

435   Towards the end of the melt season 2021, a major rainfall episode (Fig. 4, ③) clearly has some impact on p at the multi-day

time scale (Fig. 4d, Fig. 6a) and coincides with a considerable glacier acceleration. During this event, the $p - Q$ relationship

indicates that the drainage system evolves in a transient manner (class III, Fig. 6a). Prior to this event, Q was at low levels for a

period of about 10 days (Fig. 4d), and presumably, the capacity of the drainage system had decreased, when it suddenly become

overwhelmed by the arrival of water volumes. This results in a sharp increase of p, provoking a short-term acceleration of the

440   glacier. Similar late season events have also been reported in other studies (Andrews et al., 2014; Rada and Schoof, 2018).

5.2.2   The melt season 2022: long duration and high intensity

In contrast to the melt season 2021, the melt season 2022 is long (at least, 83 days since our records end before the melt

season ceases) and contains frequent and large excursions of runoff Q above 20 m^3 s^{-1} (Fig. 4a). Applying our interpretation

scheme to the observed responses of water pressure, p, channel-flow-induced seismic power, P, hydraulic radius, R, and the

445   hydraulic gradient, S at the seasonal scale (Fig. 5), yields a picture of the subglacial drainage system that differs from the one

in the preceding year (Section 5.2.1). The $R - Q$ relationship is linearly positive, indicating drainage system size evolving at

equilibrium with Q (Fig. 5g). The $S - Q$ relationship follows a trajectory that first is typical of a steady-state channel (Fig. 5h,

1) before bending over to a positive slope similar to that expected for a rigid pipe (Fig. 5h, 2, 3 and 4). Such behavior is typical

for a system that is continuously overwhelmed since the subglacial channels cannot adapt fast enough to increasing Q. $P - Q$

450   relationship in 2022 shows similar behavior as in 2021, if we account for that the 2022 record does not cover the falling limb

of Q (Fig. 5f). The view of a continuously overwhelmed drainage system is further supported by the generally positive slope

of the $p - Q$ relationship which has a considerably smaller clockwise hysteresis compared to the preceding year (Fig. 5i).

On shorter time scales, the classifications of $R - Q$ and $S - Q$ exhibit similar behavior as in 2021 (Fig. 6b and 8b), indicative

for system adjustment also on multi-day and diurnal scales. However, the class II behavior of $S - Q$ in the beginning of the

455   melt season visible in Figure 6b, remains difficult to explain. On a diurnal time scale, the dominance of class IV in the $S - Q$

relation before July 2022 suggests that channels evolution are in equilibrium with Q (Fig. 8b). It then displays a switch to

mainly class I behavior which in turn, is indicative of a transient evolution, typical for a drainage system that cannot adapt fast

enough to the runoff variations. $R - Q$ relationship exhibits a similar switch (from class III to class II 8b) with implications

consistent to the interpretation above. The class I behavior of $p - Q$ on multi-day scales further supports the view of geometric

460   adjustment at this scale. The same analysis on the diurnal scale (Fig. 8b) reveals a blurry picture that is hard to interpret which

we ascribe to a lack of major diurnal variations of p during the melt season 2022 (Fig. 4d).

5.2.3   Ambiguous interpretation from borehole and cryoseismic records

In the previous section, we interpreted the multi-variable record in terms of drainage system evolution in response to runoff

(summarised in Figure 10). We note that sometimes, interpretations derived from different records are ambiguous: for instance,

465   during the melt season 2021, on a seasonal scale, the relationships between the cryoseismic records (P, R and S) and Q yield

a picture of a subglacial drainage system in equilibrium with Q. In contrast, the $p - Q$ relationship based on the borehole

record is symptomatic of a transient evolution where geometric adjustments lag variations in Q. Another example is found in

the analysis of diurnal variations in 2022 (Fig. 8b) where the cryoseismic records indicate a switch from an equilibrium to a transient evolution coinciding with a major increase in Q (Fig. 8d ⑥). The corresponding classification of the $p-Q$ relation

470   is less conclusive about a similar switch and exhibits variations over all classes with no clearly recognizable pattern. In this section, we discuss potential sources for these inconsistencies and how these may be resolved.

The scaling relationships used for benchmarking the cryoseismological records (P, R and S) have been derived for ice-walled channels in a hard-bed configuration (Röthlisberger, 1972). However, Kongsvegen glacier rests on a soft bed and properties of its subglacial drainage system may yield a different seismic signature. For instance, for a soft base, it has been

475   proposed that drainage can occur through ice-roofed canals incised in the sediment (Walder and Fowler, 1994) or through a macroporous horizon, i.e. a quasi-continuous sheet of water and sediment (Flowers and Clarke, 2002). For both configurations, drainage capacity will evolve similar to that of ice-walled channels, whose cross-sectional geometry is determined by melt-opening and creep-closure. However, the dynamics of geometric adjustments comprises the additional processes of till erosion and creep which may act on a different time scale and thus render different cross-sectional geometries. One of the underlying

480   assumptions of the applied scaling framework (Gimbert et al., 2016; Nanni et al., 2020) is that flow depth is considerably larger than the wall roughness, neglecting the seismogenic influence of roughness. However, for very wide and shallow drainage networks at a soft bed this assumption may be violated. Instead, for such a sheet-like drainage configuration (Creyts and Schoof, 2009), geometric adjustments can take place at the scale of roughness; therefore, roughness alterations represent additional influence on channel-flow-induced seismic power, in addition to those by hydraulic radius and hydraulic gradient.

485   Similar alterations of roughness at diurnal time scales has been proposed by Schuler and Fischer (2003) to explain patterns of hydrodynamic dispersion observed in multi-temporal tracer tests.

Perceiving the drainage system as a macroporous sheet goes along with spatial heterogeneity, with parts of the glacier base being located in areas that are well connected to the main water drainage, whereas other parts only indirectly communicate with that system (Murray and Clarke, 1995), for instance through a porous medium of lower permeability. Such a situation

490   would apply when interpreting records from sensors that are physically installed at different locations along the base (e.g., in different boreholes), but also, when the viewfield of the individual sensors differs such that the recorded signals have different characteristics of noise and signal amplitude. In our case, P integrates the seismicity in the 3-10 Hz frequency band in which seismic wavelengths are on the order of 150-500m (for typical surface wave velocity on the order of 1500 m sec^{-1} Köhler et al., 2012; Gimbert et al., 2021b). Accordingly, the cryoseismologically derived variables P, R and S are sensitive to an area

495   of ~1 km^2 around the geophone location, and therefore, they will always represent the hydraulically most active part within this area.

In contrast, water pressure p is measured at the bottom of the borehole, the precise dimensions of which at the base of the glacier are unknown, but estimated to be ~ 20 cm in diameter. Depending on the hydraulic connection of the borehole and the nature of the surrounding drainage system, p may be representative for about 1 m^2 in case of hydraulic isolation, or for a

500   several orders of magnitude larger area in case of a direct connection to a widespread drainage system. Resuming the idea of a macroporous sheet aids resolving the apparent discrepancies derived from the different records: if the active drainage system within 1 km^2 around our instrument site is in equilibrium with Q, the seismological record would reveal this, whereas the

borehole record may reveal a different interpretation if the borehole itself is located in a less-well connected or even isolated part of the glacier bed. The apparent discrepancy derived from different records therefore supports the comprehension of the

505 drainage system as a macroporous, spatially heterogeneous sheet. Although the minor diurnal variability of p during the melt season 2022 may be interpreted as symptomatic for hydraulic isolation, p displays seasonal variability responding to Q. This observation suggests that differently connected parts of the glacier bed hydraulically communicate, at least when the capacity of the drainage is overwhelmed in times of high water supply. During such episodes, high water pressures would occur over a large part of the glacier bed, possibly promoting glacier sliding. Indeed, during the melt season 2022, several speed-up episodes

510 are recorded during episodes of high Q that coincided with p close to overburden pressure (Fig. 4 b ⑥, ⑦), even though the borehole is not well connected to the main drainage system.

5.3 Till changes and glacier dynamics

Above (Sect. 5.1), we have proposed an interpretation scheme based on the phase relationship between the force experienced by the ploughmeter, F and the pore water pressure of the till, here taken as adequately represented by p. We explore two

515 alternative rheologies for the till, each having a different $p - F$ signature. A Coulomb-plastic till would emanate in a negative relationship, whereas for a viscous till, one would expect a positive slope in the $p - F$ relationship (Fig. 10).

On a seasonal scale during the melt seasons, the $p - F$ relation displays a generally negative slope (Figs. 5e and j and 9a). For a Coulomb-plastic material, an increase in pore water pressure results in a decrease in shear strength, which in turn would cause a decrease in F (Fig. 10). Furthermore, the observed anti-correlation between p and F is in good agreement with the modeling

520 results of Kavanaugh and Clarke (2006) for a Coulomb-plastic material, an interpretation that is in line with the findings of Fischer and Clarke (1994); Fischer et al. (1998, 2001) at Trapridge glacier, Storglaciären and Unteraargletscher respectively. However, during winter 2021/22, the $p - F$ relationship exhibits a positive slope (Fig. 9a), a behavior that may be indicative for viscous till behavior. Nevertheless, in our interpretation of viscous behavior we have assumed a positive relationship between p and sliding velocity, but we do not observe such an acceleration during winter. Instead, we propose that the co-variation of

525 p and F stems from a consolidation of the till in the hydraulically inactive season, when a reduction in pore space causes both an increase in water pressure as well as an increase in ploughing resistance (Fig. 10).

On shorter time scales, time series of p and F exhibit complex behavior: correlation (Fig. 9b), anti-correlation (Fig. 9c) and lagging after each other occur (Fig. 9d). Applying our interpretation scheme suggests that during episodes similar to those pictured in Fig. 9b, till behaves as a viscous material (Fig. 10), whereas in other situations (Fig. 9c), it has characteristics of a

530 Coulomb-plastic rheology (Fig. 10).

As discussed above, we infer viscous behavior from a positive $p - F$ relation because we associate a positive relation between sliding velocity and water pressure, a relation which is well established, called shear thickening (Mari et al., 2014). Shear thickening is caused by the temporary aggregation of particles in response to increase in stress that leads to the increase in flow resistance thus, viscosity. Indeed, in our records, we find viscous behaviour typically, but not exclusively, during high

535 velocity episodes (Figs. 4b ① and 9b). Outside of speed-up episode scenarios, the till can behave as a viscous material due to the collision of the ploughmeter and a big clast, favoring the aggregation of particles around it (Fig. 10). The occurrence of
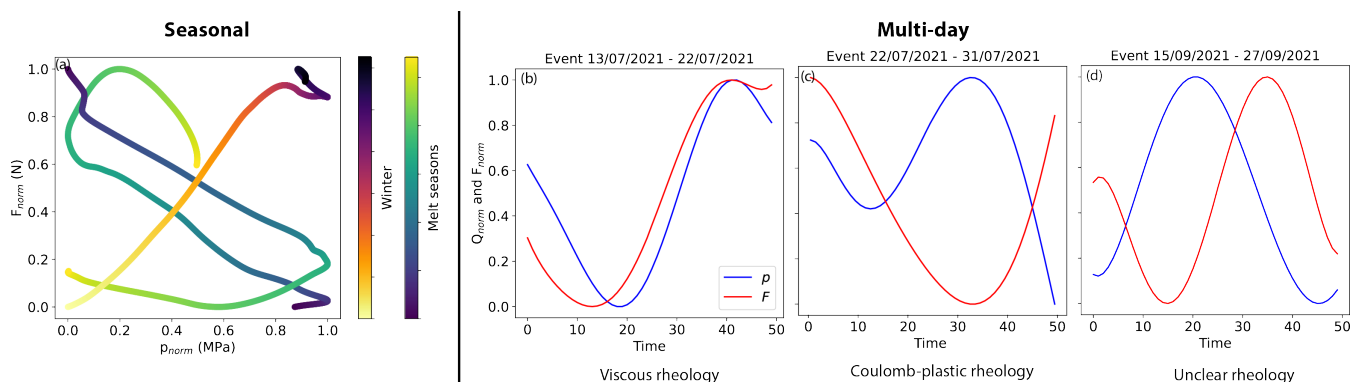
Figure 9. Comparison between the variations of water pressure p and ploughmeter force F (a) at the seasonal, and (b) to (d) multi-day time scales. (a) Relationship between p and F at the seasonal time scale. Blue-yellow and yellow-purple color scales indicate time during melt seasons and winter, respectively. (b) Evolution of F (red curve) and p (blue curve) for one event where the till behaves like a viscous material. This event is an example of the relationship between Q and F. A similar behaviour has been observed during two events (from July 13, 2021 to July 22, 2021; August 8, 2021 to August 17, 2021). (c) Evolution of F (red curve) and p (blue curve) for one event where the till behaves like a Coulomb-plastic material. This event is an example of the relationship between Q and F. A similar behaviour has been observed during three events (from July 22, 2021 to July 31, 2021; from July 7, 2021 to August 8, 2021 and from July 11, 2022 to July 23, 2022). (d) Evolution of F (red curve) and p (blue curve) for one event where the till rheology is unclear. This event is an example of the relationship between Q and F. A similar behaviour has been observed during two events (from September 15, 2021 to September 27, 2021; from May 28, 2022 to June 6, 2022). Multi-day variations are exhibited simultaneously by F and p only for five and two events during the melt seasons 2021 and 2022. F and p are normalised between 0 and 1 in all the figures.

intermediate situations (Fig. 9d) may be interpreted as a transient between the two end-members, influenced by both viscous and Coulomb-plastic behavior but without clear dominance of one rheology.

This renders a picture of complex till mechanical evolution: on long time scales, there is a dominance of Coulomb-plastic behavior, possibly further influenced by till consolidation and dilatation. At the same time, viscous behavior may be latent, but on shorter time scales, such as during speed-up events, this may be the dominating control on force experienced by the ploughmeter. To our knowledge, such complex behavior has not been reported before.

6 Conclusions

In this study, we adopt a multi-method, multi-scale analysis to examine the responses of the subglacial environment to changes in runoff. We synthesize the broad spectrum of behaviors in four classes and interpret these in terms of drainage system evolution and till rheology (Fig. 10).

Our records cover two contrasting melt seasons: during the short and less intensive melt season 2021, we conjecture that our borehole intersected a well-connected part of the subglacial drainage system, whereas in the longer and intensive melt season

2022, the borehole records characteristics of a poorly connected subdomain of the glacier bed (Fig. 10). Nevertheless, seismo-
logical records indicate the existence of an efficient drainage system in both periods, thereby suggesting the co-existence of
both configurations (Fig. 10). Considering the different footprints of different sensors, complementary information can be ob-
tained that allows the composition of a consistent picture of the subglacial environment. To further investigate the hydrological
conditions at the base of Kongsvegen, more information on the interactions between the active and less-well connected parts
of the bed could be inferred from a dense seismic array (Nanni et al., 2021).

The phase relationship analysis of the force exerted on the ploughmeter and the water pressure reveals complex till rheol-
ogy. At long time scales, the till is behaving mainly as Coulomb-plastic material while at shorter time scale, the till exhibits
behaviour of a viscous material, especially but not systematically during glacier accelerations, or as Coulomb-plastic material
(Fig. 10). The mechanical conditions assessed with the ploughmeter record in our study could be complemented by assessing
changes in till properties using seismic noise interferometry (Zhan, 2019).

In this study, we show the importance of a multi-sensor multi-scale approach to study the complex variations of hydro-
mechanical conditions in response to runoff changes. Such approach may also be beneficial for understanding the dynamic of
other transient geological systems. Such systems are characterized by stress and internal structures that build up and evolve
over decades and where rapid movement can be initiated by short-lived events or by destabilization of a small portion of the
studied system leading to its partial or complete failure, such as glacial surges or collapses, volcanic eruptions, landslides, or
earthquakes.
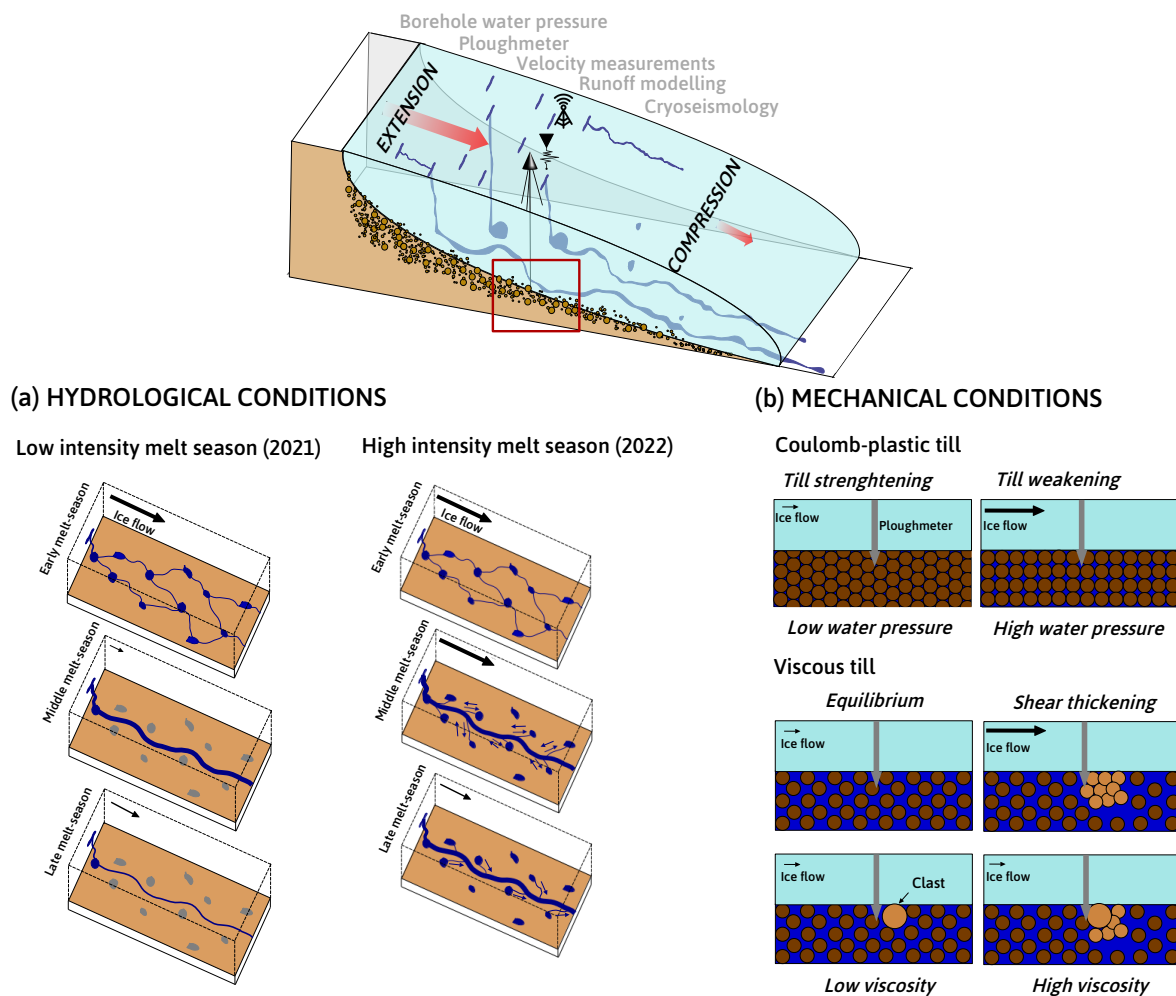
Figure 10. Schematic of the adjustment of hydro-mechanical conditions to variations in runoff between the period spanning from June 2021 to August 2022. (a) Hydrological proxies, i.e. water pressure (p), hydraulic gradient (S), and hydraulic radius (R), were used to analyze the evolution of the subglacial drainage system during the short and low intensity melt season of 2021, and the long and high intensity melt season of 2022. Our findings indicate that during the former season, the subglacial drainage system adapted to runoff changes in steady-state, leading to an increase in its capacity over time. However, during the latter season, we observed a transient evolution of the drainage system in response to the sudden and high-intensity input of runoff. As a result, the drainage capacity of the main active channels was exceeded, causing water to leak into poorly connected areas of the bed and increasing the water pressure, thereby triggering speed-up events. (b) The mechanical proxy, i.e., force (F), was used to examine the rheological behaviors of the sediment. Our results revealed that the till rheology behaved as a Coulomb-plastic material or a viscous material. For a Coulomb-plastic rheology, the force and water pressure show anti-correlated behavior. This indicates that the till strengthened at low water pressure but weakened at high water pressure. For a viscous rheology, the viscosity of the till increases as the shear rate increases (shear thickening, Mari et al., 2014). Shear thickening is caused by the formation of temporary particle networks or clusters within the fluid, which increase in size and strength under higher stress and lead to increased resistance to flow (Mari et al., 2014). This behaviour is enhanced by speed-up episodes or the heterogeneity of the grain size in the till.

Code and data availability. The data are uploaded in Zenodo (https://doi.org/10.5281/zenodo.7648444, Bouchayer (2023a)) and the code to reproduce the figures in the manuscript can be found on GitHub (https://github.com/Colinebouch/mammamia_alldata_processing, Bouchayer (2023b)).

Author contributions. CB, UN and TVS designed the concept of the study. CB developed the code, produced all tables and figures and wrote
570   the initial draft. UN and TVS provided help and ideas in all phases of the study and wrote parts of the manuscript. FR provided ideas and feedbacks that lead to the finalisation of the manuscript. TVS provided all the organizational and technical support. JK and TVS provided the logistical support to conduct the field campaigns. JH built the ploughmeter. CB, UN, JH, TVS, PML and JK conducted fieldwork. TVS and CB processed the ploughmeter and water pressure data. UN and CB processed the seismic data. PML processed the GNSS velocity data. JK provided the long term velocity data at KNG6. LS contributed with CARRA and AROME-ARCTIC forcing, and simulated surface runoff.
575   All authors contributed to the final manuscript with input and suggestions.

Competing interests. The authors declare no conflict of interest.

Acknowledgements. This project has received support from the Research Council of Norway through the projects MAMMAMIA (grant no. 301837) and SLIDE (no. 337228) and from the Faculty of Mathematics and Natural Sciences at the University of Oslo through the strategic research initiative EarthFlows. We are grateful to the Governor of Svalbard for permitting fieldwork at Kongsvegen. The energetic help of
580   Wenxue Cao, Ceslav Czyk, Basile De Fleurian, Jean-Charles Gallet, Adrien Gilbert, Stephen Hudson, Simon Filhol, Urs Fischer, Catherine Larose, and Ashley Morris during the field campaigns is greatly acknowledged.UN acknowledges Andreas Köhler for support in the seismic analysis.

References

Alley, R.: Water-pressure coupling of sliding and bed deformation: II. Velocity-depth profiles, Journal of Glaciology, 35, 119–129, 1989.

Alley, R. B.: Multiple steady states in ice-water-till systems, Annals of Glaciology, 14, 1–5, 1990.

Alley, R. B., Blankenship, D. D., Bentley, C. R., and Rooney, S.: Deformation of till beneath ice stream B, West Antarctica, Nature, 322, 57–59, 1986.

Andrews, L. C., Catania, G. A., Hoffman, M. J., Gulley, J. D., Lüthi, M. P., Ryser, C., Hawley, R. L., and Neumann, T. A.: Direct observations of evolving subglacial drainage beneath the Greenland Ice Sheet, Nature, 514, 80–83, 2014.

Bartholomaus, T. C., Amundson, J. M., Walter, J. I., O'Neel, S., West, M. E., and Larsen, C. F.: Subglacial discharge at tidewater glaciers revealed by seismic tremor, Geophysical research letters, 42, 6391–6398, 2015.

Benn, D., Fowler, A. C., Hewitt, I., and Sevestre, H.: A general theory of glacier surges, Journal of Glaciology, 65, 701–716, 2019.

Björnsson, H., Gjessing, Y., Hamran, S.-E., Hagen, J. O., LiestøL, O., Pálsson, F., and Erlingsson, B.: The thermal regime of sub-polar glaciers mapped by multi-frequency radio-echo sounding, Journal of Glaciology, 42, 23–32, 1996.

Bouchayer, C.: Dataset at a 3h resolution used in the paper 'The MAMMAMIA project: A multi-scale multi- method approach to understand runoff-induced changes in the subglacial environment and consequences for surge dynamic in Kongsvegen glacier, Svalbard', https://doi.org/10.5281/zenodo.7648444, 2023a.

Bouchayer, C.: GitHub repository to process the data, published in Zenodo, https://github.com/Colinebouch/mammamia_alldata_processing/commits/v1.0, https://doi.org/10.5281/zenodo.7648470, last update: 17/02/2022, 2023b.

Boulton, G. and Hindmarsh, R.: Sediment deformation beneath glaciers: rheology and geological consequences, Journal of Geophysical Research: Solid Earth, 92, 9059–9082, 1987.

Boulton, G., Dobbie, K., and Zatsepin, S.: Sediment deformation beneath glaciers and its coupling to the subglacial hydraulic system, Quaternary International, 86, 3–28, 2001.

Clarke, G. K.: Subglacial processes, Annu. Rev. Earth Planet. Sci., 33, 247–276, 2005.

Creyts, T. T. and Schoof, C. G.: Drainage through subglacial water sheets, Journal of Geophysical Research: Earth Surface, 114, 2009.

Damsgaard, A., Goren, L., and Suckale, J.: Water pressure fluctuations control variability in sediment flux and slip dynamics beneath glaciers and ice streams, Communications Earth & Environment, 1, 66, 2020.

Davison, B. J., Sole, A. J., Livingstone, S. J., Cowton, T. R., and Nienow, P. W.: The influence of hydrology on the dynamics of land-terminating sectors of the Greenland ice sheet, Frontiers in Earth Science, 7, 10, 2019.

Doyle, S. H., Hubbard, B., Christoffersen, P., Young, T. J., Hofstede, C., Bougamont, M., Box, J., and Hubbard, A.: Physical conditions of fast glacier flow: 1. Measurements from boreholes drilled to the bed of Store Glacier, West Greenland, Journal of Geophysical Research: Earth Surface, 123, 324–348, 2018.

Fischer, U. H. and Clarke, G. K.: Ploughing of subglacial sediment, Journal of Glaciology, 40, 97–106, 1994.

Fischer, U. H., Iverson, N. R., Hanson, B., Hooke, R. L., and Jansson, P.: Estimation of hydraulic properties of subglacial till from plough-meter measurements, Journal of Glaciology, 44, 517–522, 1998.

Fischer, U. H., Clarke, G. K., and Blatter, H.: Evidence for temporally varying "sticky spots" at the base of Trapridge Glacier, Yukon Territory, Canada, Journal of Glaciology, 45, 352–360, 1999.

Fischer, U. H., Porter, P. R., Schuler, T., Evans, A. J., and Gudmundsson, G. H.: Hydraulic and mechanical properties of glacial sediments beneath Unteraargletscher, Switzerland: implications for glacier basal motion, Hydrological Processes, 15, 3525–3540, 2001.

620   Flowers, G. E.: Modelling water flow under glaciers and ice sheets, Proceedings of the Royal Society A: Mathematical, Physical and Engi-
neering Sciences, 471, 20140 907, 2015.

Flowers, G. E. and Clarke, G. K.: A multicomponent coupled model of glacier hydrology 1. Theory and synthetic examples, Journal of
Geophysical Research: Solid Earth, 107, ECV–9, 2002.

Fudge, T., Humphrey, N. F., Harper, J. T., and Pfeffer, W. T.: Diurnal fluctuations in borehole water levels: configuration of the drainage
625   system beneath Bench Glacier, Alaska, USA, Journal of Glaciology, 54, 297–306, 2008.

Gilbert, A., Gimbert, F., Thøgersen, K., Schuler, T. V., and Kääb, A.: A Consistent Framework for Coupling Basal Friction With Subglacial
Hydrology on Hard-Bedded Glaciers, Geophysical Research Letters, 49, e2021GL097 507, 2022.

Gimbert, F., Tsai, V. C., Amundson, J. M., Bartholomaus, T. C., and Walter, J. I.: Subseasonal changes observed in subglacial channel
pressure, size, and sediment transport, Geophysical Research Letters, 43, 3786–3794, 2016.

630   Gimbert, F., Gilbert, A., Gagliardini, O., Vincent, C., and Moreau, L.: Do existing theories explain seasonal to multi-decadal changes in
glacier basal sliding speed?, Geophysical Research Letters, 48, e2021GL092 858, 2021a.

Gimbert, F., Nanni, U., Roux, P., Helmstetter, A., Garambois, S., Lecointre, A., Walpersdorf, A., Jourdain, B., Langlais, M., Laarman, O.,
et al.: A multi-physics experiment with a temporary dense seismic array on the Argentière glacier, French Alps: The RESOLVE project,
Seismological Society of America, 92, 1185–1201, 2021b.

635   Gordon, S., Sharp, M., Hubbard, B., Smart, C., Ketterling, B., and Willis, I.: Seasonal reorganization of subglacial drainage inferred from
measurements in boreholes, Hydrological Processes, 12, 105–133, 1998.

Hagen, J. O., Liestøl, O., Roland, E., and Jørgensen, T.: Glacier atlas of Svalbard and jan mayen, vol. 129, Norsk Polarinstitutt Oslo, 1993.

Hansen, D. and Zoet, L.: Characterizing sediment flux of deforming glacier beds, Journal of Geophysical Research: Earth Surface, 127,
e2021JF006 544, 2022.

640   Hjelle, A.: Geology of Svalbard, 1993.

Hoffman, M. J., Andrews, L. C., Price, S. F., Catania, G. A., Neumann, T. A., Lüthi, M. P., Gulley, J., Ryser, C., Hawley, R. L., and Morriss,
B.: Greenland subglacial drainage evolution regulated by weakly connected regions of the bed, Nature communications, 7, 13 903, 2016.

Hoffmann, K.: Applying the wheatstone bridge circuit, HBM Germany, 1974.

Hooke, R. L., Laumann, T., and Kohler, J.: Subglacial water pressures and the shape of subglacial conduits, Journal of Glaciology, 36, 67–71,
645   1990.

Hooke, R. L., Hanson, B., Iverson, N. R., Jansson, P., and Fischer, U. H.: Rheology of till beneath Storglaciären, Sweden, Journal of
Glaciology, 43, 172–179, 1997.

Hubbard, B., Sharp, M., Willis, I., Nielsen, M., and Smart, C.: Borehole water-level variations and the structure of the subglacial hydrological
system of Haut Glacier d'Arolla, Valais, Switzerland, Journal of Glaciology, 41, 572–583, 1995.

650   Humphrey, N., Kamb, B., Fahnestock, M., and Engelhardt, H.: Characteristics of the bed of the lower Columbia Glacier, Alaska, Journal of
Geophysical Research: Solid Earth, 98, 837–846, 1993.

Iken, A.: The effect of the subglacial water pressure on the sliding velocity of a glacier in an idealized numerical model, Journal of Glaciology,
27, 407–421, 1981.

Iken, A. and Bindschadler, R. A.: Combined measurements of subglacial water pressure and surface velocity of Findelengletscher, Switzer-
655   land: conclusions about drainage system and sliding mechanism, Journal of Glaciology, 32, 101–119, 1986.

Iken, A. and Truffe, M.: The relationship between subglacial water pressure and velocity of Findelengletscher, Switzerland, during its advance
and retreat, Journal of Glaciology, 43, 328–338, 1997.

Iverson, N. R., Jansson, P., and Hooke, R. L.: In-situ measurement of the strength of deforming subglacial till, Journal of Glaciology, 40, 497–503, 1994.

660 Iverson, N. R., Hanson, B., Hooke, R. L., and Jansson, P.: Flow mechanism of glaciers on soft beds, Science, 267, 80–81, 1995.

Iverson, N. R., Hooyer, T. S., and Baker, R. W.: Ring-shear studies of till deformation: Coulomb-plastic behavior and distributed strain in glacier beds, Journal of Glaciology, 44, 634–642, 1998.

Javed, A., Hamshaw, S. D., Lee, B. S., and Rizzo, D. M.: Multivariate event time series analysis using hydrological and suspended sediment data, Journal of Hydrology, 593, 125 802, 2021.

665 Kamb, B.: Glacier surge mechanism based on linked cavity configuration of the basal water conduit system, Journal of Geophysical Research: Solid Earth, 92, 9083–9100, 1987.

Kamb, B. and Engelhardt, H.: Antarctic ice stream B: conditions controlling its motions and interactions with the climate system, IAHS Publication, 208, 145–154, 1991.

Kavanaugh, J. L. and Clarke, G. K.: Evidence for extreme pressure pulses in the subglacial water system, Journal of Glaciology, 46, 206–212, 670 2000.

Kavanaugh, J. L. and Clarke, G. K.: Discrimination of the flow law for subglacial sediment using in situ measurements and an interpretation model, Journal of Geophysical Research: Earth Surface, 111, 2006.

Köhler, A., Chapuis, A., Nuth, C., Kohler, J., and Weidle, C.: Autonomous detection of calving-related seismicity at Kronebreen, Svalbard, The Cryosphere, 6, 393–406, 2012.

675 Labedz, C. R., Bartholomaus, T. C., Amundson, J. M., Gimbert, F., Karplus, M. S., Tsai, V. C., and Veitch, S. A.: Seismic mapping of subglacial hydrology reveals previously undetected pressurization event, Journal of Geophysical Research: Earth Surface, 127, e2021JF006 406, 2022.

Lenton, T. M., Held, H., Kriegler, E., Hall, J. W., Lucht, W., Rahmstorf, S., and Schellnhuber, H. J.: Tipping elements in the Earth's climate system, Proceedings of the national Academy of Sciences, 105, 1786–1793, 2008.

680 Liestøl, O.: The glaciers in the Kongsfjorden area, Spitsbergen, Norsk Geografisk Tidsskrift-Norwegian Journal of Geography, 42, 231–238, 1988.

Lindner, F., Walter, F., Laske, G., and Gimbert, F.: Glaciohydraulic seismic tremors on an Alpine glacier, The Cryosphere, 14, 287–308, 2020.

Lliboutry, L.: General theory of subglacial cavitation and sliding of temperate glaciers, Journal of Glaciology, 7, 21–58, 1968.

685 Maier, N., Gimbert, F., and Gillet-Chaulet, F.: Threshold response to melt drives large-scale bed weakening in Greenland, Nature, 607, 714–720, 2022.

Mari, R., Seto, R., Morris, J. F., and Denn, M. M.: Shear thickening, frictionless and frictional rheologies in non-Brownian suspensions, Journal of Rheology, 58, 1693–1724, 2014.

Meier, M. F. and Post, A.: What are glacier surges?, Canadian Journal of Earth Sciences, 6, 807–817, https://doi.org/10.1139/e69-081, 1969.

690 Melvold, K. and Hagen, J. O.: Evolution of a surge-type glacier in its quiescent phase: Kongsvegen, Spitsbergen, 1964–95, Journal of Glaciology, 44, 394–404, 1998.

Millstein, J. D., Minchew, B. M., and Pegler, S. S.: Ice viscosity is more sensitive to stress than commonly assumed, Communications Earth & Environment, 3, 57, 2022.

Minchew, B. M. and Meyer, C. R.: Dilation of subglacial sediment governs incipient surge motion in glaciers with deformable beds, Pro-
695 ceedings of the Royal Society A, 476, 20200 033, 2020.

Moon, T., Ahlstrøm, A., Goelzer, H., Lipscomb, W., and Nowicki, S.: Rising oceans guaranteed: Arctic land ice loss and sea level rise, Current climate change reports, 4, 211–222, 2018.

Müller, M., Homleid, M., Ivarsson, K. I., Køltzow, M. A., Lindskog, M., Midtbø, K. H., Andrae, U., Aspelien, T., Berggren, L., Bjørge, D., Dahlgren, P., Kristiansen, J., Randriamampianina, R., Ridal, M., and Vignes, O.: AROME-MetCoOp: A nordic convective-scale operational weather prediction model, Weather and Forecasting, 32, 609–627, https://doi.org/10.1175/WAF-D-16-0099.1, 2017.

Murray, T. and Clarke, G. K.: Black-box modeling of the subglacial water system, Journal of Geophysical Research: Solid Earth, 100, 10 231–10 245, 1995.

Murray, T. and Porter, P. R.: Basal conditions beneath a soft-bedded polythermal surge-type glacier: Bakaninbreen, Svalbard, Quaternary International, 86, 103–116, 2001.

Nanni, U., Gimbert, F., Vincent, C., Gräff, D., Walter, F., Piard, L., and Moreau, L.: Quantification of seasonal and diurnal dynamics of subglacial channels using seismic observations on an Alpine glacier, The Cryosphere, 14, 1475–1496, 2020.

Nanni, U., Gimbert, F., Roux, P., and Lecointre, A.: Observing the subglacial hydrology network and its dynamics with a dense seismic array, Proceedings of the National Academy of Sciences, 118, e2023757 118, 2021.

Nienow, P., Sole, A., Slater, D. A., and Cowton, T.: Recent advances in our understanding of the role of meltwater in the Greenland Ice Sheet system, Current Climate Change Reports, 3, 330–344, 2017.

Nye, J. F.: Water flow in glaciers: jökulhlaups, tunnels and veins, Journal of Glaciology, 17, 181–207, 1976.

Podolskiy, E. A. and Walter, F.: Cryoseismology, Reviews of geophysics, 54, 708–758, 2016.

Porter, P. R., Murray, T., and Dowdeswell, J. A.: Sediment deformation and basal dynamics beneath a glacier surge front: Bakaninbreen, Svalbard, Annals of Glaciology, 24, 21–26, 1997.

Pörtner, H.-O., Roberts, D. C., Masson-Delmotte, V., Zhai, P., Tignor, M., Poloczanska, E., and Weyer, N.: The ocean and cryosphere in a changing climate, IPCC special report on the ocean and cryosphere in a changing climate, 1155, 2019.

Rada, C. and Schoof, C.: Channelized, distributed, and disconnected: subglacial drainage under a valley glacier in the Yukon, The Cryosphere, 12, 2609–2636, 2018.

Rada Giacaman, C. A. and Schoof, C.: Channelized, distributed, and disconnected: spatial structure and temporal evolution of the subglacial drainage under a valley glacier in the Yukon, The Cryosphere, 17, 761–787, https://doi.org/10.5194/tc-17-761-2023, 2023.

RGI, C.: Randolph Glacier Inventory (RGI) - A dataset of Global Glacier Outlines: Version 6.0, http://www.glims.org/RGI/randolph60.html, 2017.

Röthlisberger, H.: Water pressure in intra-and subglacial channels, Journal of Glaciology, 11, 177–203, 1972.

Rothlisberger, H.: Glacial hydrology, Glacio-fluvial sediment transfer, 1987.

Rounce, D. R., Hock, R., Maussion, F., Hugonnet, R., Kochtitzky, W., Huss, M., Berthier, E., Brinkerhoff, D., Compagno, L., Copland, L., et al.: Global glacier change in the 21st century: Every increase in temperature matters, Science, 379, 78–83, 2023.

Schmidt, L. S., Schuler, T. V., Thomas, E. E., and Westermann, S.: Meltwater runoff and glacier mass balance in the high Arctic: 1991–2022 simulations for Svalbard, EGUsphere, pp. 1–32, 2023.

Schoof, C.: Ice-sheet acceleration driven by melt supply variability, Nature, 468, 803–806, 2010.

Schuler, T. and Fischer, U. H.: Elucidating changes in the degree of tracer dispersion in a subglacial channel, Annals of Glaciology, 37, 275–280, 2003.

Schyberg, H., Yang, X., Køltzow, M., Amstrup, B., Bakketun, å., Bazile, E., Bojarova, J., Box, J., Dahlgren, P., Hagelin, S., Homleid, M., Horányi, A., Høyer, J., Johansson, å., Killie, M., Körnich, H., Le Moigne, P., Lindskog, M., Manninen, T., Nielsen Englyst, P., and Wang,

Z.: Arctic regional reanalysis on single levels from 1991 to present, Copernicus Climate Change Service (C3S) Climate Data Store (CDS), https://doi.org/10.24381/cds.713858f6, 2020.

Stocker, T.: Climate change 2013: the physical science basis: Working Group I contribution to the Fifth assessment report of the Intergovernmental Panel on Climate Change, Cambridge university press, 2014.

Sugiyama, S., Skvarca, P., Naito, N., Enomoto, H., Tsutaki, S., Tone, K., Marinsek, S., and Aniya, M.: Ice speed of a calving glacier modulated by small fluctuations in basal water pressure, Nature Geoscience, 4, 597–600, 2011.

Sugiyama, S., Navarro, F. J., Sawagaki, T., Minowa, M., Segawa, T., Onuma, Y., Otero, J., and Vasilenko, E. V.: Subglacial water pressure and ice-speed variations at Johnsons Glacier, Livingston Island, Antarctic Peninsula, Journal of Glaciology, 65, 689–699, 2019.

Terleth, Y., Van Pelt, W. J., Pohjola, V. A., and Pettersson, R.: Complementary approaches towards a universal model of glacier surges, Frontiers in Earth Science, 9, 732 962, 2021.

Thøgersen, K., Gilbert, A., Schuler, T. V., and Malthe-Sørenssen, A.: Rate-and-state friction explains glacier surge propagation, Nature communications, 10, 1–8, https://doi.org/10.1038/s41467-019-10506-4, 2019.

Truffer, M., Kääb, A., Harrison, W. D., Osipova, G. B., Nosenko, G. A., Espizua, L., Gilbert, A., Fischer, L., Huggel, C., and Burns, P. A. C. e. a.: Glacier surges, in: Snow and Ice-Related Hazards, Risks, and Disasters, pp. 417–466, Elsevier, 2021.

Tsai, V. C., Smith, L. C., Gardner, A. S., and Seroussi, H.: A unified model for transient subglacial water pressure and basal sliding, Journal of Glaciology, 68, 390–400, 2022.

Tulaczyk, S., Kamb, W. B., and Engelhardt, H. F.: Basal mechanics of ice stream B, West Antarctica: 1. Till mechanics, Journal of Geophysical Research: Solid Earth, 105, 463–481, 2000.

Walder, J. S. and Fowler, A.: Channelized subglacial drainage over a deformable bed, Journal of glaciology, 40, 3–15, 1994.

Warburton, K., Hewitt, D., and Neufeld, J.: Shear dilation of subglacial till results in time-dependent sliding laws, Proceedings of the Royal Society A, 479, 20220 536, 2023.

Weertman, J. et al.: Catastrophic glacier advances, 1962.

Westermann, S., Ingeman-Nielsen, T., Scheer, J., Aalstad, K., Aga, J., Chaudhary, N., Etzelmüller, B., Filhol, S., Kääb, A., Renette, C., et al.: The CryoGrid community model (version 1.0)–a multi-physics toolbox for climate-driven simulations in the terrestrial cryosphere, Geoscientific Model Development Discussions, pp. 1–61, 2022.

Woodward, J., Murray, T., and McCaig, A.: Formation and reorientation of structure in the surge-type glacier Kongsvegen, Svalbard, Journal of Quaternary Science: Published for the Quaternary Research Association, 17, 201–209, 2002.

Yang, X., Nielsen, K. P., Amstrup, B., Peralta, C., Høyer, J., Englyst, P. N., Schyberg, H., Homleid, M., Kpltzow, M. ø., Randriamampianina, R., Dahlgren, P., Stpylen, E., Valkonen, T., Palmason, B., Thorsteinsson, S., Bojarova, J., Körnich, H., Lindskog, M., Box, J., and Mankoff, K.: C3S Arctic regional reanalysis – Full system documentation, Tech. rep., 2021.

Zhan, Z.: Seismic noise interferometry reveals transverse drainage configuration beneath the surging Bering Glacier, Geophysical Research Letters, 46, 4747–4756, 2019.

Zoet, L. K. and Iverson, N. R.: A slip law for glaciers on deformable beds, Science, 368, 76–78, 2020.

Zoet, L. K., Iverson, N. R., Andrews, L., and Helanow, C.: Transient evolution of basal drag during glacier slip, Journal of Glaciology, 68, 741–750, 2022.

Appendix A: Surface velocity data

770   The velocity record presented in this study has been composed from two different GNSS records. One of the GNSS stations is positioned at stake 6 (KNG-6: 13.15153^oE 78.78067^oN) and the other one at stake 7 (KNG-7: 13.23962^oE 78.76770^oN). In figure A1, we present the two datasets that has been combined. We apply a one-week moving median for KNG7 velocity to smooth the record especially during the winter period when the velocities are low and thus the daily velocity derivation is less accurate.
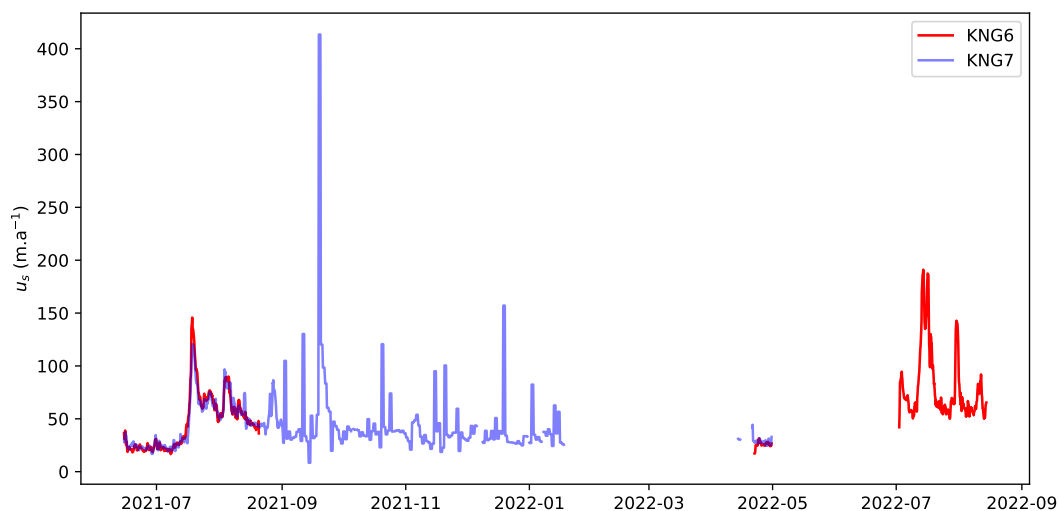
Figure A1. Velocity data series from KNG6 (red curve) and KNG7 (blue curve) GNSS stations.

Appendix B: Events

Table B1. Description of the twelve multi-day time scale events during the melt season 2021

Event	Start	Stop	Duration
0	2021-07-01 00:00:00	2021-07-03 03:00:00	2 days 03:00:00
1	2021-07-03 03:00:00	2021-07-13 06:00:00	10 days 03:00:00
2	2021-07-13 06:00:00	2021-07-22 03:00:00	8 days 21:00:00
3	2021-07-22 03:00:00	2021-07-31 03:00:00	9 days 00:00:00
4	2021-07-31 03:00:00	2021-08-08 12:00:00	8 days 09:00:00
5	2021-08-08 12:00:00	2021-08-17 21:00:00	9 days 09:00:00
6	2021-08-17 21:00:00	2021-08-28 00:00:00	10 days 03:00:00
7	2021-08-28 00:00:00	2021-09-04 15:00:00	7 days 15:00:00
8	2021-09-04 15:00:00	2021-09-15 21:00:00	11 days 06:00:00
9	2021-09-15 21:00:00	2021-09-27 03:00:00	11 days 06:00:00
10	2021-09-27 03:00:00	2021-10-04 12:00:00	7 days 09:00:00
11	2021-10-04 12:00:00	2021-10-04 21:00:00	0 days 09:00:00

Table B2. Description of the eight multi-day time scale events during the melt season 2022

Event	Start	Stop	Duration
0	2022-05-25 00:00:00	2022-05-28 21:00:00	3 days 21:00:00
1	2022-05-28 21:00:00	2022-06-10 12:00:00	12 days 15:00:00
2	2022-06-10 12:00:00	2022-06-26 06:00:00	15 days 18:00:00
3	2022-06-26 06:00:00	2022-07-11 06:00:00	15 days 00:00:00
4	2022-07-11 06:00:00	2022-07-23 18:00:00	12 days 12:00:00
5	2022-07-23 18:00:00	2022-08-07 18:00:00	15 days 00:00:00
6	2022-08-07 18:00:00	2022-08-16 00:00:00	8 days 06:00:00
7	2022-08-16 00:00:00	2022-08-16 15:00:00	0 days 15:00:00

Table B3. Description of the 96 diurnal time scale events during the melt season 2021

Event	Start	Stop	Duration	Event	Start	Stop	Duration
0	2021-07-01 00:00:00	2021-07-02 09:00:00	1 days 09:00:00	36	2021-08-06 12:00:00	2021-08-07 03:00:00	0 days 15:00:00
1	2021-07-02 09:00:00	2021-07-03 18:00:00	1 days 09:00:00	37	2021-08-07 03:00:00	2021-08-07 15:00:00	0 days 12:00:00
2	2021-07-03 18:00:00	2021-07-04 15:00:00	0 days 21:00:00	38	2021-08-07 15:00:00	2021-08-08 15:00:00	1 days 00:00:00
3	2021-07-04 15:00:00	2021-07-05 15:00:00	1 days 00:00:00	39	2021-08-08 15:00:00	2021-08-09 15:00:00	1 days 00:00:00
4	2021-07-05 15:00:00	2021-07-06 15:00:00	1 days 00:00:00	40	2021-08-09 15:00:00	2021-08-10 15:00:00	1 days 00:00:00
5	2021-07-06 15:00:00	2021-07-07 15:00:00	1 days 00:00:00	41	2021-08-10 15:00:00	2021-08-11 15:00:00	1 days 00:00:00
6	2021-07-07 15:00:00	2021-07-08 18:00:00	1 days 03:00:00	42	2021-08-11 15:00:00	2021-08-12 15:00:00	1 days 00:00:00
7	2021-07-08 18:00:00	2021-07-09 09:00:00	0 days 15:00:00	43	2021-08-12 15:00:00	2021-08-13 12:00:00	0 days 21:00:00
8	2021-07-09 09:00:00	2021-07-10 15:00:00	1 days 06:00:00	44	2021-08-13 12:00:00	2021-08-14 12:00:00	1 days 00:00:00
9	2021-07-10 15:00:00	2021-07-11 12:00:00	0 days 21:00:00	45	2021-08-14 12:00:00	2021-08-15 15:00:00	1 days 03:00:00
10	2021-07-11 12:00:00	2021-07-12 12:00:00	1 days 00:00:00	46	2021-08-15 15:00:00	2021-08-16 06:00:00	0 days 15:00:00
11	2021-07-12 12:00:00	2021-07-13 18:00:00	1 days 06:00:00	47	2021-08-16 06:00:00	2021-08-16 18:00:00	0 days 12:00:00
12	2021-07-13 18:00:00	2021-07-14 15:00:00	0 days 21:00:00	48	2021-08-16 18:00:00	2021-08-17 18:00:00	1 days 00:00:00
13	2021-07-14 15:00:00	2021-07-15 15:00:00	1 days 00:00:00	49	2021-08-17 18:00:00	2021-08-18 15:00:00	0 days 21:00:00
14	2021-07-15 15:00:00	2021-07-16 12:00:00	0 days 21:00:00	50	2021-08-18 15:00:00	2021-08-19 15:00:00	1 days 00:00:00
15	2021-07-16 12:00:00	2021-07-17 15:00:00	1 days 03:00:00	51	2021-08-19 15:00:00	2021-08-20 18:00:00	1 days 03:00:00
16	2021-07-17 15:00:00	2021-07-18 15:00:00	1 days 00:00:00	52	2021-08-20 18:00:00	2021-08-21 18:00:00	1 days 00:00:00
17	2021-07-18 15:00:00	2021-07-19 15:00:00	1 days 00:00:00	53	2021-08-21 18:00:00	2021-08-22 15:00:00	0 days 21:00:00
18	2021-07-19 15:00:00	2021-07-20 12:00:00	0 days 21:00:00	54	2021-08-22 15:00:00	2021-08-24 12:00:00	1 days 21:00:00
19	2021-07-20 12:00:00	2021-07-21 12:00:00	1 days 00:00:00	55	2021-08-24 12:00:00	2021-08-25 15:00:00	1 days 03:00:00
20	2021-07-21 12:00:00	2021-07-22 15:00:00	1 days 03:00:00	56	2021-08-25 15:00:00	2021-08-26 09:00:00	0 days 18:00:00
21	2021-07-22 15:00:00	2021-07-23 12:00:00	0 days 21:00:00	57	2021-08-26 09:00:00	2021-08-27 15:00:00	1 days 06:00:00
22	2021-07-23 12:00:00	2021-07-24 12:00:00	1 days 00:00:00	58	2021-08-27 15:00:00	2021-08-28 15:00:00	1 days 00:00:00
23	2021-07-24 12:00:00	2021-07-25 12:00:00	1 days 00:00:00	59	2021-08-28 15:00:00	2021-08-29 15:00:00	1 days 00:00:00
24	2021-07-25 12:00:00	2021-07-26 12:00:00	1 days 00:00:00	60	2021-08-29 15:00:00	2021-08-30 12:00:00	0 days 21:00:00
25	2021-07-26 12:00:00	2021-07-27 15:00:00	1 days 03:00:00	61	2021-08-30 12:00:00	2021-08-31 12:00:00	1 days 00:00:00
26	2021-07-27 15:00:00	2021-07-28 15:00:00	1 days 00:00:00	62	2021-08-31 12:00:00	2021-09-01 09:00:00	0 days 21:00:00
27	2021-07-28 15:00:00	2021-07-29 12:00:00	0 days 21:00:00	63	2021-09-01 09:00:00	2021-09-02 06:00:00	0 days 21:00:00
28	2021-07-29 12:00:00	2021-07-30 12:00:00	1 days 00:00:00	64	2021-09-02 06:00:00	2021-09-04 09:00:00	2 days 03:00:00
29	2021-07-30 12:00:00	2021-07-31 15:00:00	1 days 03:00:00	65	2021-09-04 09:00:00	2021-09-05 03:00:00	0 days 18:00:00
30	2021-07-31 15:00:00	2021-08-01 12:00:00	0 days 21:00:00	66	2021-09-05 03:00:00	2021-09-06 00:00:00	0 days 21:00:00
31	2021-08-01 12:00:00	2021-08-02 12:00:00	1 days 00:00:00	67	2021-09-06 00:00:00	2021-09-06 15:00:00	0 days 15:00:00
32	2021-08-02 12:00:00	2021-08-03 06:00:00	0 days 18:00:00	68	2021-09-06 15:00:00	2021-09-07 03:00:00	0 days 12:00:00
33	2021-08-03 06:00:00	2021-08-04 12:00:00	1 days 06:00:00	69	2021-09-07 03:00:00	2021-09-08 00:00:00	0 days 21:00:00
34	2021-08-04 12:00:00	2021-08-05 12:00:00	1 days 00:00:00	70	2021-09-08 00:00:00	2021-09-08 18:00:00	0 days 18:00:00
35	2021-08-05 12:00:00	2021-08-06 12:00:00	1 days 00:00:00	71	2021-09-08 18:00:00	2021-09-09 18:00:00	1 days 00:00:00

Table B3. (Following) Description of the 96 diurnal time scale events during the melt season 2021

Event	Start	Stop	Duration
72	2021-09-09 18:00:00	2021-09-10 18:00:00	1 days 00:00:00
73	2021-09-10 18:00:00	2021-09-11 09:00:00	0 days 15:00:00
74	2021-09-11 09:00:00	2021-09-12 06:00:00	0 days 21:00:00
75	2021-09-12 06:00:00	2021-09-13 03:00:00	0 days 21:00:00
76	2021-09-13 03:00:00	2021-09-14 09:00:00	1 days 06:00:00
77	2021-09-14 09:00:00	2021-09-15 06:00:00	0 days 21:00:00
78	2021-09-15 06:00:00	2021-09-19 00:00:00	3 days 18:00:00
79	2021-09-19 00:00:00	2021-09-20 12:00:00	1 days 12:00:00
80	2021-09-20 12:00:00	2021-09-22 15:00:00	2 days 03:00:00
81	2021-09-22 15:00:00	2021-09-23 06:00:00	0 days 15:00:00
82	2021-09-23 06:00:00	2021-09-24 09:00:00	1 days 03:00:00
83	2021-09-24 09:00:00	2021-09-25 18:00:00	1 days 09:00:00
84	2021-09-25 18:00:00	2021-09-27 00:00:00	1 days 06:00:00
85	2021-09-27 00:00:00	2021-09-27 12:00:00	0 days 12:00:00
86	2021-09-27 12:00:00	2021-09-28 03:00:00	0 days 15:00:00
87	2021-09-28 03:00:00	2021-09-29 03:00:00	1 days 00:00:00
88	2021-09-29 03:00:00	2021-09-29 18:00:00	0 days 15:00:00
89	2021-09-29 18:00:00	2021-09-30 09:00:00	0 days 15:00:00
90	2021-09-30 09:00:00	2021-10-01 03:00:00	0 days 18:00:00
91	2021-10-01 03:00:00	2021-10-02 18:00:00	1 days 15:00:00
92	2021-10-02 18:00:00	2021-10-03 12:00:00	0 days 18:00:00
93	2021-10-03 12:00:00	2021-10-04 00:00:00	0 days 12:00:00
94	2021-10-04 00:00:00	2021-10-04 15:00:00	0 days 15:00:00
95	2021-10-04 15:00:00	2021-10-04 21:00:00	0 days 06:00:00

8

Table B4. Description of the 85 diurnal time scale events during the melt season 2022

Event	Start	Stop	Duration	Event	Start	Stop	Duration
0	2022-05-25 00:00:00	2022-05-25 06:00:00	0 days 06:00:00	36	2022-06-29 12:00:00	2022-06-30 12:00:00	1 days 00:00:00
1	2022-05-25 06:00:00	2022-05-26 12:00:00	1 days 06:00:00	37	2022-06-30 12:00:00	2022-07-01 12:00:00	1 days 00:00:00
2	2022-05-26 12:00:00	2022-05-27 03:00:00	0 days 15:00:00	38	2022-07-01 12:00:00	2022-07-02 06:00:00	0 days 18:00:00
3	2022-05-27 03:00:00	2022-05-27 18:00:00	0 days 15:00:00	39	2022-07-02 06:00:00	2022-07-03 12:00:00	1 days 06:00:00
4	2022-05-27 18:00:00	2022-05-28 15:00:00	0 days 21:00:00	40	2022-07-03 12:00:00	2022-07-04 12:00:00	1 days 00:00:00
5	2022-05-28 15:00:00	2022-05-29 15:00:00	1 days 00:00:00	41	2022-07-04 12:00:00	2022-07-05 09:00:00	0 days 21:00:00
6	2022-05-29 15:00:00	2022-05-30 15:00:00	1 days 00:00:00	42	2022-07-05 09:00:00	2022-07-06 09:00:00	1 days 00:00:00
7	2022-05-30 15:00:00	2022-05-31 15:00:00	1 days 00:00:00	43	2022-07-06 09:00:00	2022-07-07 09:00:00	1 days 00:00:00
8	2022-05-31 15:00:00	2022-06-01 12:00:00	0 days 21:00:00	44	2022-07-07 09:00:00	2022-07-08 09:00:00	1 days 00:00:00
9	2022-06-01 12:00:00	2022-06-02 15:00:00	1 days 03:00:00	45	2022-07-08 09:00:00	2022-07-09 09:00:00	1 days 00:00:00
10	2022-06-02 15:00:00	2022-06-03 12:00:00	0 days 21:00:00	46	2022-07-09 09:00:00	2022-07-10 12:00:00	1 days 03:00:00
11	2022-06-03 12:00:00	2022-06-04 09:00:00	0 days 21:00:00	47	2022-07-10 12:00:00	2022-07-11 09:00:00	0 days 21:00:00
12	2022-06-04 09:00:00	2022-06-05 15:00:00	1 days 06:00:00	48	2022-07-11 09:00:00	2022-07-12 06:00:00	0 days 21:00:00
13	2022-06-05 15:00:00	2022-06-06 18:00:00	1 days 03:00:00	49	2022-07-12 06:00:00	2022-07-13 06:00:00	1 days 00:00:00
14	2022-06-06 18:00:00	2022-06-07 12:00:00	0 days 18:00:00	50	2022-07-13 06:00:00	2022-07-14 12:00:00	1 days 06:00:00
15	2022-06-07 12:00:00	2022-06-08 15:00:00	1 days 03:00:00	51	2022-07-14 12:00:00	2022-07-15 09:00:00	0 days 21:00:00
16	2022-06-08 15:00:00	2022-06-09 18:00:00	1 days 03:00:00	52	2022-07-15 09:00:00	2022-07-16 09:00:00	1 days 00:00:00
17	2022-06-09 18:00:00	2022-06-10 18:00:00	1 days 00:00:00	53	2022-07-16 09:00:00	2022-07-17 09:00:00	1 days 00:00:00
18	2022-06-10 18:00:00	2022-06-11 15:00:00	0 days 21:00:00	54	2022-07-17 09:00:00	2022-07-18 09:00:00	1 days 00:00:00
19	2022-06-11 15:00:00	2022-06-12 15:00:00	1 days 00:00:00	55	2022-07-18 09:00:00	2022-07-19 09:00:00	1 days 00:00:00
20	2022-06-12 15:00:00	2022-06-13 15:00:00	1 days 00:00:00	56	2022-07-19 09:00:00	2022-07-20 09:00:00	1 days 00:00:00
21	2022-06-13 15:00:00	2022-06-14 15:00:00	1 days 00:00:00	57	2022-07-20 09:00:00	2022-07-21 09:00:00	1 days 00:00:00
22	2022-06-14 15:00:00	2022-06-15 15:00:00	1 days 00:00:00	58	2022-07-21 09:00:00	2022-07-22 09:00:00	1 days 00:00:00
23	2022-06-15 15:00:00	2022-06-16 15:00:00	1 days 00:00:00	59	2022-07-22 09:00:00	2022-07-23 06:00:00	0 days 21:00:00
24	2022-06-16 15:00:00	2022-06-17 18:00:00	1 days 03:00:00	60	2022-07-23 06:00:00	2022-07-24 09:00:00	1 days 03:00:00
25	2022-06-17 18:00:00	2022-06-18 12:00:00	0 days 18:00:00	61	2022-07-24 09:00:00	2022-07-25 06:00:00	0 days 21:00:00
26	2022-06-18 12:00:00	2022-06-19 15:00:00	1 days 03:00:00	62	2022-07-25 06:00:00	2022-07-26 09:00:00	1 days 03:00:00
27	2022-06-19 15:00:00	2022-06-21 15:00:00	2 days 00:00:00	63	2022-07-26 09:00:00	2022-07-27 09:00:00	1 days 00:00:00
28	2022-06-21 15:00:00	2022-06-22 12:00:00	0 days 21:00:00	64	2022-07-27 09:00:00	2022-07-28 09:00:00	1 days 00:00:00
29	2022-06-22 12:00:00	2022-06-23 09:00:00	0 days 21:00:00	65	2022-07-28 09:00:00	2022-07-29 09:00:00	1 days 00:00:00
30	2022-06-23 09:00:00	2022-06-24 12:00:00	1 days 03:00:00	66	2022-07-29 09:00:00	2022-07-30 06:00:00	0 days 21:00:00
31	2022-06-24 12:00:00	2022-06-25 12:00:00	1 days 00:00:00	67	2022-07-30 06:00:00	2022-07-31 09:00:00	1 days 03:00:00
32	2022-06-25 12:00:00	2022-06-26 12:00:00	1 days 00:00:00	68	2022-07-31 09:00:00	2022-08-01 06:00:00	0 days 21:00:00
33	2022-06-26 12:00:00	2022-06-27 15:00:00	1 days 03:00:00	69	2022-08-01 06:00:00	2022-08-02 09:00:00	1 days 03:00:00
34	2022-06-27 15:00:00	2022-06-28 09:00:00	0 days 18:00:00	70	2022-08-02 09:00:00	2022-08-03 09:00:00	1 days 00:00:00
35	2022-06-28 09:00:00	2022-06-29 12:00:00	1 days 03:00:00	71	2022-08-03 09:00:00	2022-08-04 06:00:00	0 days 21:00:00

Table B4. (Following) Description of the 85 diurnal time scale events during the melt season 2022

Event	Start	Stop	Duration
72	2022-08-04 06:00:00	2022-08-05 09:00:00	1 days 03:00:00
73	2022-08-05 09:00:00	2022-08-06 09:00:00	1 days 00:00:00
74	2022-08-06 09:00:00	2022-08-07 09:00:00	1 days 00:00:00
75	2022-08-07 09:00:00	2022-08-08 09:00:00	1 days 00:00:00
76	2022-08-08 09:00:00	2022-08-09 09:00:00	1 days 00:00:00
77	2022-08-09 09:00:00	2022-08-10 09:00:00	1 days 00:00:00
78	2022-08-10 09:00:00	2022-08-11 09:00:00	1 days 00:00:00
79	2022-08-11 09:00:00	2022-08-12 09:00:00	1 days 00:00:00
80	2022-08-12 09:00:00	2022-08-13 09:00:00	1 days 00:00:00
81	2022-08-13 09:00:00	2022-08-14 09:00:00	1 days 00:00:00
82	2022-08-14 09:00:00	2022-08-15 12:00:00	1 days 03:00:00
83	2022-08-15 12:00:00	2022-08-16 09:00:00	0 days 21:00:00
84	2022-08-16 09:00:00	2022-08-16 15:00:00	0 days 06:00:00

Appendix C: Spectrogram

Large seasonal changes in channel-flow-induced seismic power, P are observed within the 3–10 Hz frequency range, in which P is higher by more than two orders of magnitude during the melt season (mid-May to September) compared to winter (Fig. C1). Changes in P are also observed within the 10–20 Hz frequency range, with P during the melt season being about an order

780   of magnitude larger than in winter (Fig. C1).
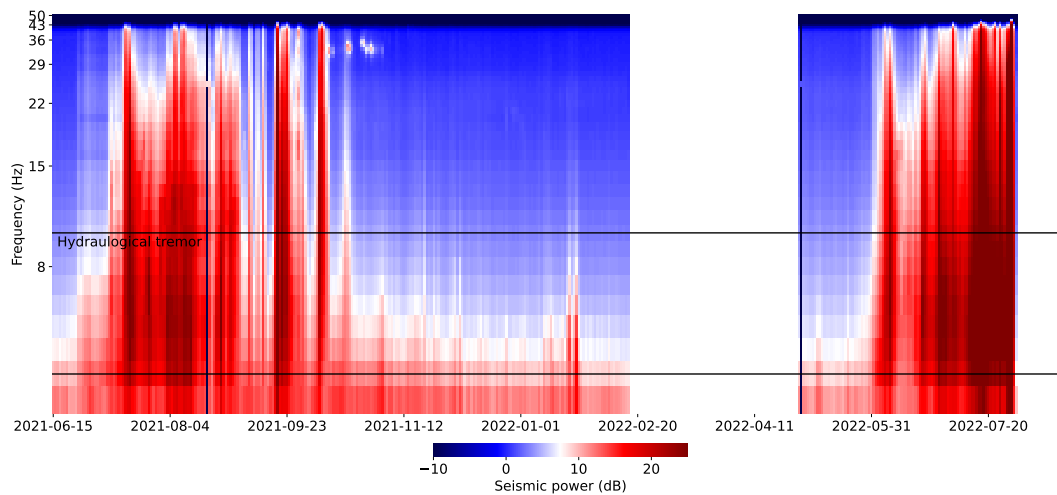
Figure C1. Spectrogram of the observed channel-flow-induced seismic power P as a function of time on the x-axis and frequency on the y-axis. Colours represent channel-flow-induced seismic power on a decimal logarithmic scale. White bands are data gaps. The two black lines delineate the frequency band between 3 and 10 Hz that we used in this study.

Appendix D: Metrics used in the classification

Figure D1 provides a visual representation of the metrics used to classify the events.
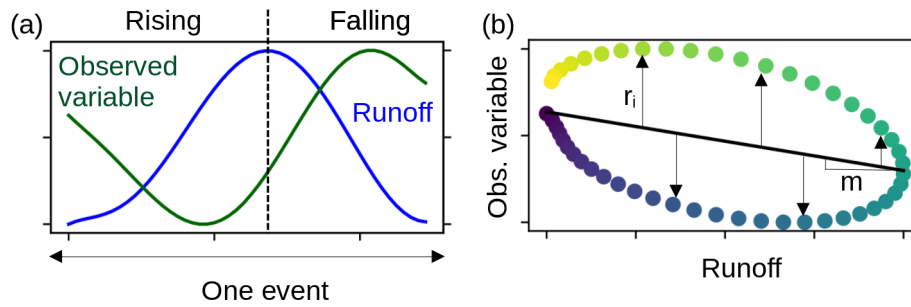
Figure D1. Description of the metrics used to classify the events. (a) Description of one event with the rising and falling part of the runoff to calculate the hysteresis θ. (b) The linear fit used to calculate the residual sum of squares RSS and its slope, m.

Appendix E: Band pass-filtered time series

We have filtered the original time series to determine the different frequency signatures separately. For the seasonal scale, we have applied a low-pass filter with a cutoff at 20 days (Fig. E1 a). For the multi-day scale, we have applied a band-pass filter between four and eight days (Fig. E1 b). For the daily time-scale, we have applied a band-pass filter between six hours and 36 hours (Fig. E1 b).
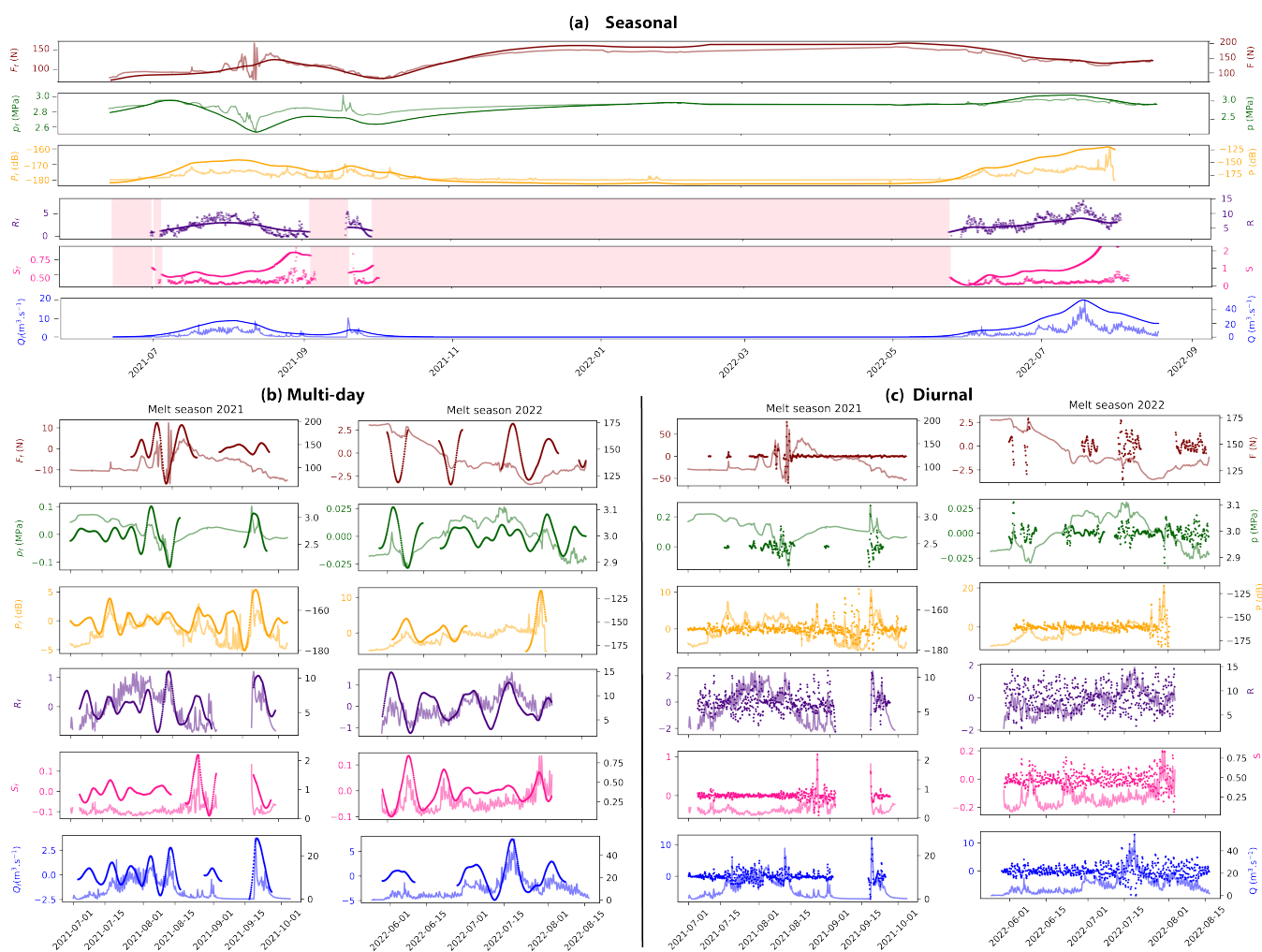
Figure E1. Band-pass filtered series for (a) seasonal (>20 days), multi-day (four to eight days) and diurnal (6h to 36h) time scales. For the last two series, we have computed the band-pass time series for the melt season time period only.

Appendix F: Frequency content of the time series between 6h and 10 days

Figure F1 shows the frequency content of all variables over the recording period between a period of 6h and a period of 10
790 days. While the force and the water pressure have only episodic frequency content on the scale of one day, the other variables
exhibit longer periods with variations on that time scale, but still concentrated during the melting season.
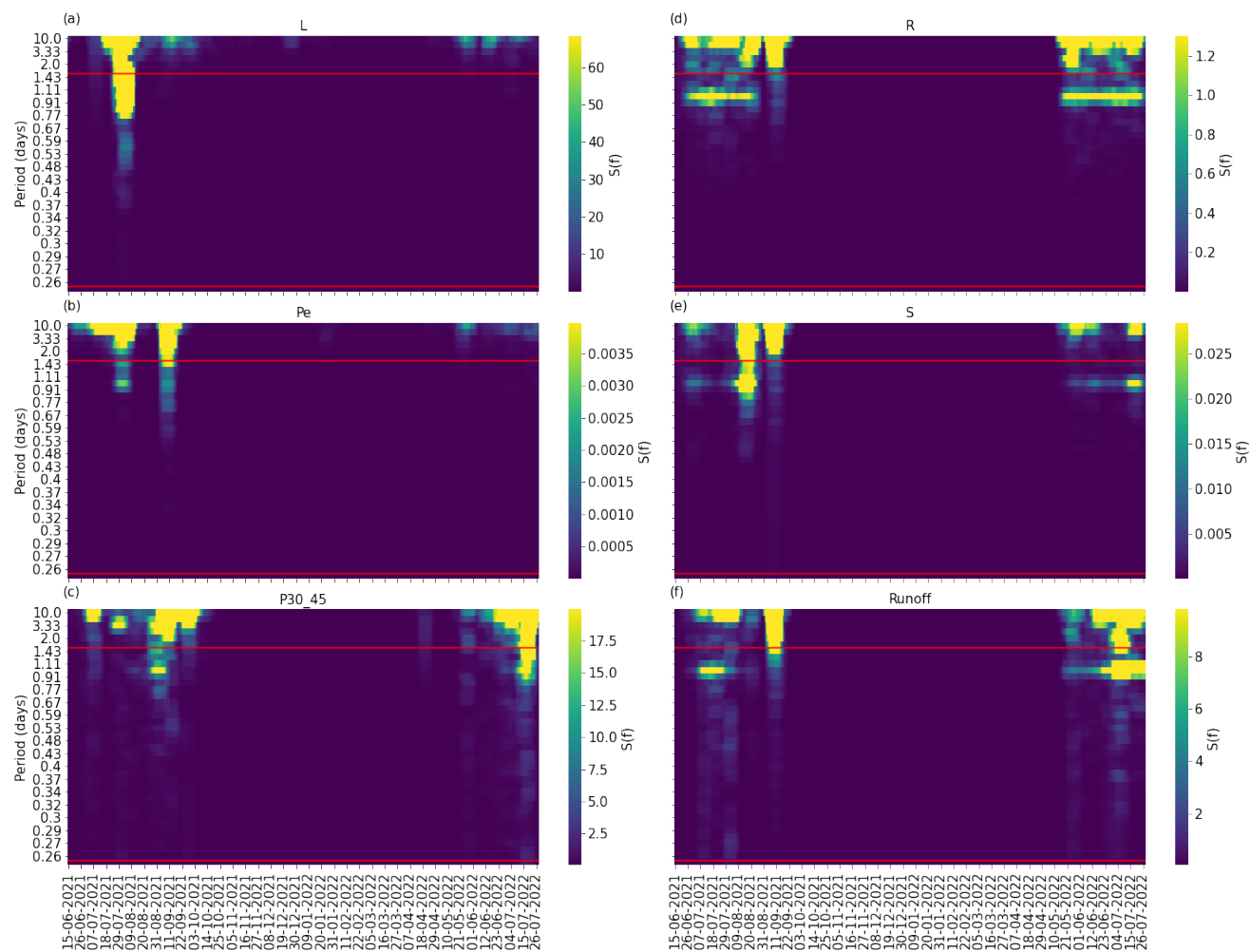
Figure F1. Frequency content intensity for all the variables between 6h an 10 days over the year. The red lines delineate the diurnal frequency
content (between 6h and 36h).